# Acoustic phonon scattering from particles embedded in an anisotropic medium: A molecular dynamics study

Neil Zuckerman and Jennifer R. Lukes
*Department of Mechanical Engineering and Applied Mechanics, University of Pennsylvania, Philadelphia, Pennsylvania 19104, USA*
(Received 24 August 2007; revised manuscript received 6 November 2007; published 5 March 2008)

Acoustic phonon scattering from isolated nanometer-scale impurity particles embedded in anisotropic media is investigated using molecular dynamics simulation. The spectral-directional dependence of the scattering, for both longitudinal and transverse modes, is found through calculation of scattering cross sections and three-dimensional scattering phase functions for inclusions of varying sizes, shapes, and stiffnesses and for waves of different wave numbers. The technique enables direct observation of the effects of mode conversion, lattice mismatch strain, elastic anisotropy, and atomistic granularity on acoustic phonon scattering from nanoparticles. The results will be useful for the design of nanoparticle-based thermal insulating materials, for example, quantum dot superlattices for thermoelectric energy conversion.

DOI: 10.1103/PhysRevB.77.094302 PACS number(s): 63.22.−m, 66.70.−f, 63.20.kp, 46.40.Cd

## I. INTRODUCTION

Nanostructured thermoelectric materials based on superlattice arrays of thin films,[1,2] nanowires,[3–5] and quantum dots[5–8] have attracted increasing research attention in recent years because of their potential to enable dramatic efficiency increases[9–11] in solid-state cooling, heating, and direct energy conversion applications as compared to conventional thermoelectric materials. Increased efficiency is related to increased thermoelectric figure of merit $ZT$,[12]

$$ZT = \frac{S_{TE}^2 \sigma_e T_{TE}}{k_c}, \tag{1}$$

where $S_{TE}$ is the Seebeck coefficient, $\sigma_e$ is the electrical conductivity, $T_{TE}$ is the temperature, and $k_c$ is the thermal conductivity. The goal of thermoelectric materials research has thus been to increase $ZT$ by engineering materials with high $S_{TE}$, high $\sigma_e$, and low $k_c$.

Quantum dot superlattices, which are regular arrays of semiconductor nanoparticles embedded in a semiconducting host material, are potentially the most promising materials for $ZT$ enhancement.[6,13,14] These materials have recently demonstrated $ZT$ values higher than 1, and this enhancement arises primarily from the reduction of $k_c$.[6,15,16] The fundamental reasons for thermal conductivity reduction in quantum dot superlattices are still not fully understood,[17] but phonon scattering from the embedded particles, changes in the phonon dispersion relation due to nanostructuring, and quantum confinement are all likely mechanisms.[18] Phonons are quantized traveling elastic waves associated with the displacement of atoms from their equilibrium lattice positions, and their scattering from "obstacles" in their paths governs the thermal conductivity of nonmetallic solids. These obstacles include other phonons, grain boundaries, impurity atoms, structural defects such as vacancies and dislocations, changes in atomic mass (isotopes), and, in general, any features that change the bond stiffness, bond orientation, or mass of adjacent atoms from those of the host lattice. The scattering of phonons from particles is strongly affected by the ratio of particle size to phonon wavelength and by particle arrangement, both of which have a significant influence on thermal conductivity.[1,17] Recent experiments indicate that including particles of different sizes may be more effective at reducing conductivity by increasing scattering for a wide spectral range of phonons.[1] Also, for a given mass fraction of particles, a larger quantity of smaller particles may yield lower $k_c$.[19]

The scattering of phonons during these events is not spatially uniform but instead occurs preferentially in certain directions. The exact spatial distribution depends on many variables, including phonon wavelength, particle size, and particle arrangement. The ability to quantify the spectral-directional nature of scattering from embedded nanoparticles for different phonon polarizations is critically important for understanding thermal transport in quantum dot-based materials. With this knowledge, thermoelectric materials can be engineered to minimize forward scattering, and thus minimize thermal conductivity and maximize $ZT$, over the entire spectral range of phonons present in the material. The investigation described herein uses a molecular dynamics (MD) simulation to quantify this scattering in anisotropic host materials and to examine intermediate spectral ranges well removed from the analytically straightforward limiting cases of small and large wavelengths. Section II summarizes the key background information on previous work on acoustic scattering and the importance of crystal anisotropy on phonon scattering. Sections III and VII discuss the MD modeling approach developed for the present calculations and the advantages and limitations of the technique. Section IV covers the method applied to resolve mode polarizations from the simulation data. Section V presents the methodology used to calculate scattering phase functions and cross sections, Sec. VI discusses the results, and Sec. VIII summarizes the conclusions.

## II. BACKGROUND

The scattering of phonons due to impurities in crystals is a fundamentally three-dimensional problem due to the anisotropic nature of elastic waves in crystals. For a given energy, changes in phonon wave vector relative to the crystal lattice orientation will result in change in speed of phonon propa-

 

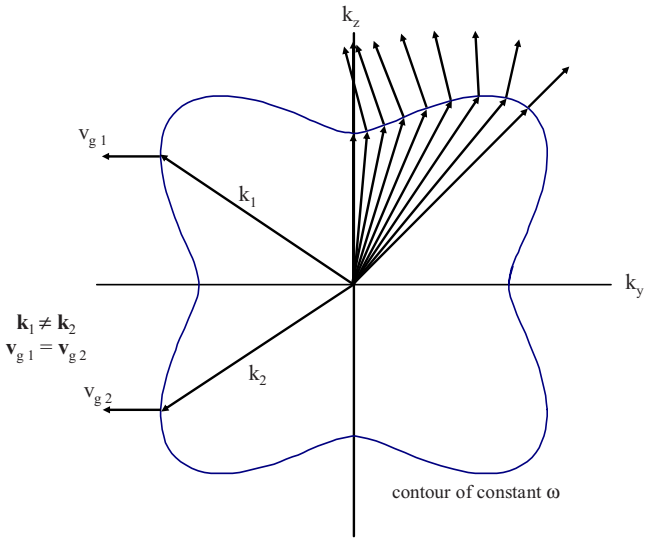


FIG. 1. (Color online) Slowness surface for quasitransverse mode in the (100) plane, plotted in $k$ space with various wave vectors and group velocity vectors, based on linear elastic equations of Auld (Ref. 36) and stiffness data of Ref. 38.

gation (or magnitude of group velocity $v_g$) as well as wave number $k$, a concept illustrated in Fig. 1. Figure 1 depicts a constant-frequency surface in wave space, showing the relationship between wave vector $\mathbf{k}$ and group velocity vector $\mathbf{v}_g$, where $\mathbf{v}_g$ will be perpendicular to the constant-frequency surface. The figure shows that a set of wave vectors with a uniform spatial distribution in $k$ space can have a very nonuniform distribution of group velocity vectors. Because of this anisotropy, when describing a scattering event in spherical coordinates, one needs to express the incoming phonon direction in terms of two angles (elevation $\theta'$ and azimuth $\phi'$) relative to the crystal lattice axes as well as two angles describing the direction of travel of the phonon after the scattering event (scattered into angular directions $\theta$ and $\phi$). Figure 2 illustrates the incident and scattered directions and the corresponding angles.

Prasher[20–24] published theoretical discussions of phonon scattering due to particles and made direct comparisons to widely used models describing the scattering of radiation, including Mie scattering, Rayleigh scattering, and scattering

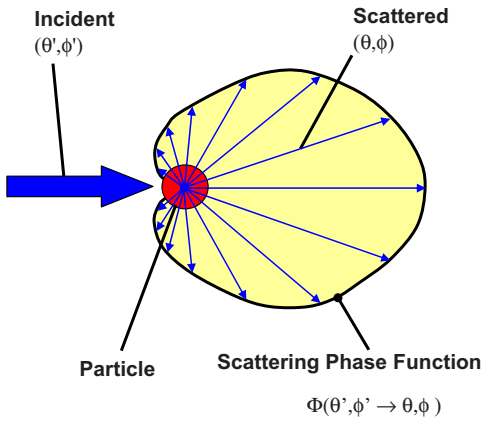


FIG. 2. (Color online) Scattering from an embedded particle.

in the geometric regime. Prasher also explained via scattering equations how wave-interference effects, dependent scattering, and multiple scattering events yield anisotropic phase functions, which can make large changes in the rate of phonon transport. These publications focused on the ultimate change in phonon propagation rate due to scattering events, described as a change in intensity, and considered calculations for conversion between two distinct modes in an *isotropic* solid.[22] Well-established phonon transport models (e.g., Ref. 25) also generally assume elastic isotropy and isotropic scattering. Existing mesoscale approaches use a cross section based on phonon wavelength and particle size, but the model equations in their final form do not track the details of the directional nature of scattering.[26] Other calculations use a more complex anisotropic phase function but do not include the details of mode conversion or the effects of material anisotropy in order to reduce the complexity of the calculations.[27] Such calculations may use directionally dependent dispersion curves for phonons, but the phase functions do not explicitly account for the relative alignment of the three-component group velocity vector and the crystal axes. While these practical approaches may be good descriptions for some one-dimensional structures (e.g., nanowires), no fully detailed mesoscale models of phonon scattering in three-dimensional structures have yet been published due to the complexity of the problem. Thus far, analytical descriptions and calculations have used anisotropic phase functions in isotropic materials.

Two types of numerical approaches are applicable to the problem of wave scattering in anisotropic elastic media: finite difference time domain (FDTD)[28] and continuum finite element modeling (FEM). The FDTD technique solves an anisotropic linear wave equation in three dimensions using a series of discrete points in space and a set of finite difference approximations. It tracks displacement at nodes in a constructed grid, with the properties of certain nodes altered to simulate an inhomogeneity (a scatterer). In the FDTD model, each region of space or set of similar nodes must be separately divided and assigned some stiffness values (represented by a matrix $\underline{\underline{C}}$). While useful for macroscopic problems, this technique will not allow the user to easily incorporate the atomic-level spatial variations in $\underline{\underline{C}}$ that occur near a nanometer-scale inclusion, as one would have to perform elaborate calculations to determine spatial variations in $\underline{\underline{C}}$ surrounding a granular, arbitrarily shaped, or nonuniform inclusion. FDTD models can provide reasonable predictions of scattering phase functions from inclusions at or above the micrometer scale and at wave numbers in the linear region of the dispersion relation (MHz-GHz range).

The other applicable approach, FEM, is commonly used to study elasticity problems and was initially investigated as a possible means to account for anisotropy effects in the present study. A drawback of continuum finite element models is their need for high spatial resolution in the finite element mesh. It was found that the extremely high mesh densities required to solve this type of three-dimensional wave-interference scattering problem made FEM impractical as a tool to study scattering in anisotropic elastic media.

The MD approach[29] addresses the deficiencies of both the FDTD and FEM approaches. This approach models materials

at an atomic level of detail and is thus easily able to capture many features that impact scattering from nanometer-scale inclusions. These key features include atomic roughness (granularity) effects, elastic stiffness variation around arbitrarily shaped inclusions, lattice mismatch/strain effects, and dispersion at large wave numbers. The approach is flexible and allows different materials, lattice constants, and geometries to be handled in an expedient manner.

The MD method described herein generates quantitative descriptions of scattering probabilities incorporating known information about the three-dimensional nature of the crystal. The model is essentially a simulation using classical mechanics of particle motion and classical wave mechanics. It does not consider those effects that are purely quantum mechanical and, as such, provides an approximate representation of the phonon-nanoparticle scattering. The approach is to calculate the parameters necessary to describe a scattering event involving the disruption of a mechanical wave in a lattice of atoms (discrete masses) connected by springlike bonds.

The terminology and equations that describe the phonon scattering events are chosen to be similar to those presently used for scattering of acoustic waves and electromagnetic radiation. For an elastic scattering event, a phonon traveling in a region containing a scatterer has a finite probability of scattering. If a phonon is described as similar to a plane wave packet traveling through the lattice, then any event that changes the phase or wave vector of the packet may be considered a scattering event. The probability of occurrence of a scattering event is described using a cross section $\Sigma_s$, which may be interpreted as being proportional to the likelihood of occurrence of a scattering event or as a description of the effective size of the scatterer as it intercepts the incoming wave. For multiple independent but identical scattering events with identical incident phonons, the total scattered energy will be proportional to $\Sigma_s$. The cross section for a single independent scattering event is a function of many variables including phonon mode, wave number, incident and outgoing angles relative to the lattice axes, lattice composition, and scatter size, shape, and material.

The likelihood of scattering into a particular direction is described with a normalized probability density function $\Phi$, known from acoustics and electromagnetics as the scattering phase function. This phase function describes the relative amount of scattered wave energy that travels in each direction, expressed per unit solid angle. The phase function may be alternatively interpreted as the relative likelihood of an incident phonon being scattered into a selected direction or span of solid angle. In addition to tracking these two parameters ($\Sigma_s$ and $\Phi$), there are multiple vibrational modes available in a solid (e.g., transverse acoustic and longitudinal acoustic), and mode conversion during scattering events is a common phenomenon, so one must track the cross section and phase function for each of these independent acoustic modes of vibration. In this discussion, we use the term "mode" to mean the same thing as wave polarization. The ratios of mode cross sections describe the relative likelihood of scattering into each of the available modes.

The existing analytical solution methods for this type of engineering problem are based on the calculation of $\Phi$ and $\Sigma_s$. The general approach of the analytical model is to evaluate a series of amplitude coefficients for scattering into various spherical harmonic modes. The phase function equations for acoustic scattering from a sphere in an isotropic solid take the form

$$\Phi(\theta) = c\sum_{n=0}^{\infty}\sum_{m=0}^{\infty}(i^n)([-i]^m)\left[A_n A_m^* P_n(\cos\theta)P_m(\cos\theta) + \frac{k_{longitudinal}}{k_{transverse}}B_n B_m^* P_n^1(\cos\theta)P_m^1(\cos\theta)\right], \quad (2)$$

where $P_n(\,)$ represents a Legendre polynomial, $P_n^1(\,)$ is an associated Legendre polynomial, and $A$ and $B$ represent harmonic mode amplitudes, which must be solved for one mode at a time as detailed in Refs. 22 and 30. The computation of $A$ and $B$ for each indexed harmonic mode $m$ or $n$ involves an evaluation of spherical Bessel functions and trigonometric functions. Prior to use, the phase function is normalized by multiplying it by some constant $c$, the value of which may be selected to make the integral over all directions $\int_{\varpi}\Phi d\varpi$ equal to a chosen constant such as 1 or $4\pi$. In many cases, this phase function is written as $\Phi(\theta,\phi)$, a confusing approach as this isotropic equation for a spherical scatterer has no $\phi$ dependence. In order to complete the calculations, the series summations must be stopped at some finite upper limits. Due to the number and type of evaluations involved, this calculation becomes impractical and prone to error as the case approaches the geometric regime ($ka_{dot} > 6$), where $a_{dot}$ is the scatterer radius. Following this calculation of $\Phi$, the scatterer cross section may be calculated as

$$\Sigma_s = 4\pi\sum_{m=0}^{\infty}\frac{1}{2m+1}\left[A_m A_m^* + (m^2+m)\frac{k_{longitudinal}}{k_{transverse}}B_m B_m^*\right], \quad (3)$$

once again truncating the series at some chosen limit.

The simpler related case of fluid acoustics is instructive in interpreting the scattering of longitudinal waves in solids, although it is not applicable to transverse waves since fluid media do not support purely wavelike motions with transverse modes. The wave energy in fluid acoustics is tracked by monitoring the fluctuation in a local gauge pressure $p$, which corresponds to wave amplitude, rather than monitoring the complete stress tensor. The group velocity $\mathbf{v}_g$ simply equals the speed of sound, and the continuous medium is isotropic. The wave intensity $\mathcal{I}$ is the measure of energy transferred per unit time per unit area and may be expressed as $\mathcal{I}=p^2/\rho v_g$ for a material with mass density $\rho$. This may be integrated over a spherical surface to obtain total energy scattered, normalized to produce $\Phi$, and divided by the incident intensity to get a scatterer cross section. For this simplified case, a number of analytically based solutions have been generated for spheres and cylinders using representation of waves as summations of spherical harmonics.[31] These solutions can be recovered from Eqs. (2) and (3) upon removal of the $B$ terms, which represent the contribution of transverse modes.

The phase functions of theoretical acoustics have distinct trends as a function of $ka_{dot}$. For large $ka_{dot}$, the geometric limit, the prediction indicates that the majority of scattered energy travels in a long, narrow lobe around the $\theta=0°$ (forward) direction. In the limit of low $ka_{dot}$, sometimes called the Rayleigh limit, the majority of the longitudinal-mode energy is backscattered in one large, almost circular lobe in the $\theta>90°$ sector, with a small, almost elliptical lobe in the forward sector. Morse and Ingard[31] provided an approximation of this shape using $\Phi(\theta)\propto(1-3\cos\theta)^2$. These features are expected to appear in the longitudinal-mode scattering phase functions from MD.

## III. SIMULATING A SCATTERING EVENT USING MOLECULAR DYNAMICS

The simulation of a scattering event is conducted using a MD model. The method used is based on the approach of Schelling *et al.*,[32] who simulated wave packet propagation and reflection in one dimension by a change in atomic mass at a planar boundary. Here, we track scattering in three dimensions from sources of many shapes and types. This kind of simulation can offer insight into the details of phonon scattering and can provide the ability to examine the behavior of individual phonons of a chosen polarization and wave vector. It allows the study of their interactions with many structures of interest, including those that have been carefully manufactured, those that occur incidentally as an uncontrolled part of material formation, and those structures that have been described but not yet physically created. Additionally, by defining pressure as $-1/3$ of the trace of the stress tensor, the methods described herein are capable of generating phase functions for acoustic materials containing only one mode of vibration and are, in theory, applicable to molecular dynamics simulations of fluid acoustics. Such studies would be useful to the nanofluids community, for example, in enabling an analysis of wave transport in fluid suspensions of nanoparticles.

To perform the simulations, a molecular dynamics model is used based on the program code of Lukes and Tien.[33] This solid inert-gas model serves as a tool to generate three-dimensional scattering data for this study, rather than as a representation of a physical system of practical interest. The model simulates a solid argon crystal in an fcc lattice, which supports acoustic modes only. The interaction of the argon atoms is computed using the 12-6 Lennard-Jones pair potential function, with parameters $\sigma=0.34$ nm and $\varepsilon=1.67\times10^{-21}$ J. The simulation of other inert gases is performed by changing these two parameters and using geometric averages of the parameters for interactions of different elements.

This structure has a lattice constant $A_{cell}$ and supports a maximum wave number of $2\pi/A_{cell}$ in the [100] direction, which is equal to $1.2\times10^{10}$ m$^{-1}$ or approximately $4/\sigma$. The lattice is configured as a box-shaped domain with rigid walls on two opposite sides and periodic boundaries on the other four sides. The lattice is initialized at a temperature of 0 K. Typical simulation cell sizes range from 10 000 to 300 000 atoms, but the method has no intrinsic limits on simulation size.

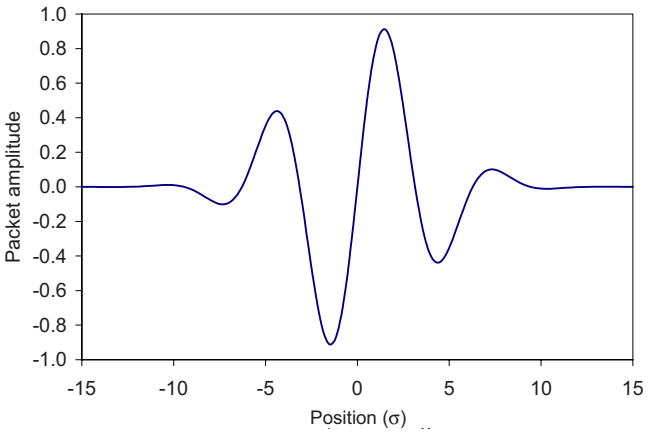


FIG. 3. (Color online) Example wave packet shape—amplitude vs position.

For purposes of modeling, the incident phonon is described as a plane wave having some displacement field $\boldsymbol{u}(\boldsymbol{r},t)$ with corresponding velocities $\boldsymbol{v}(\boldsymbol{r},t)$. The discrete pulse of the phonon is represented by a wave packet generated with some frequency $\omega$, wave number $k$, and width (or half-width), an example of which is shown in Fig. 3. The packet shape is created by multiplying a sine wave by an exponential envelope, as used by Schelling *et al.*[32] Different sections of a wave packet have slightly different values of $k$ and $\omega$, and elongating the packet in space and time can reduce this variation. The elongation of the packet requires an increase in both the number of atoms and number of time steps used in the simulation in order to avoid spurious signals at the monitoring points such as echoes from periodic nanoparticle images or reflections from the back wall of the domain. Following the scaling relations discussed near the end of this paper, this means that a packet that is twice as long in time and space will require 16 times the computational time. The goal of forming a packet with a narrow spread of $\omega$ must be balanced against the desire for more rapid computation times.

The frequency spread of each wave packet may be found by a Fourier analysis of the time history of atomic displacements, measured as the wave packet travels through a selected lattice location.[34] In practice, the wave packet becomes mildly distorted as it travels due to bond anharmonicity and numerical discretization error present in the calculations of packet initialization and propagation. Figure 4 presents a typical displacement time history measured in the MD model, showing the wave packet shape after passing through 15 lattice cells, a typical distance between the source and the scatterer in our simulations. The packet exhibits some mild trailing-edge noise. Figure 5 shows the corresponding frequency spectrum of the signal. It consists of a single Gaussian peak centered around the center frequency of 0.8 THz with a 0.33 THz full width at half maximum (FWHM). In general, the wave number spread of our packets (FWHM) falls in the range of 20%–45% of the packet's center frequency, with narrower FWHM for higher-frequency wave packets. In Fig. 5, there is a weak but visible frequency background associated with packet distortion in the anharmonic medium, but the signal outside of the primary

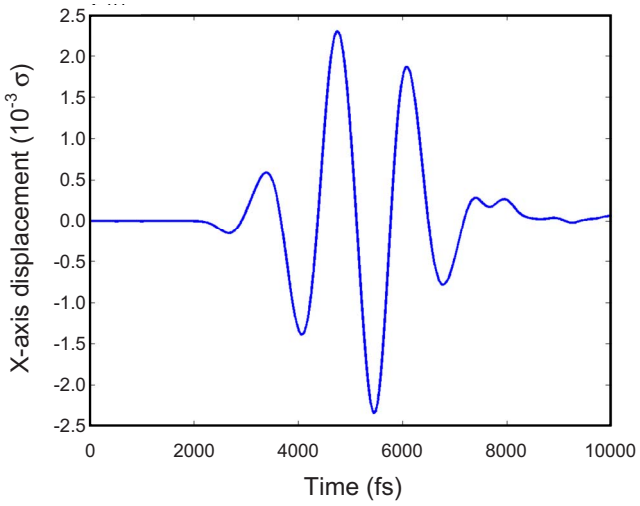


FIG. 4. (Color online) Wave packet shape measured in the center of MD model, amplitude vs position.

0.5–1.3 THz peak contains only 1.3% of the total packet energy.

Two approaches can be used to generate these packets with satisfactory results. A boundary-condition-based method functions by moving a rigid wall on the side of the simulation domain, using an exponentially damped displacement of the form $x_i(t)=x_i(0)+U\sin[\omega(t-t_{center})]e^{-\eta^2(t-t_{center})^2}$ where $x_i(t)$ represents the position of atom number $i$ at time $t$, and $U$, $\eta$, and $t_{center}$ are parameters used to control packet size and shape. Typical atomic displacements are in the range of $0.005A_{cell}$ to $0.010A_{cell}$ to ensure a linear wave behavior and reduce anharmonic packet distortion (phonon-phonon scattering) approaching the scatterer. The motion of the wall then creates a traveling wave packet in the material adjacent to the wall. A general schematic of the domain is shown in Fig. 6. Figure 7 shows the corresponding image from a section cut through an MD model with a Xe inclusion in an Ar crystal. An alternate

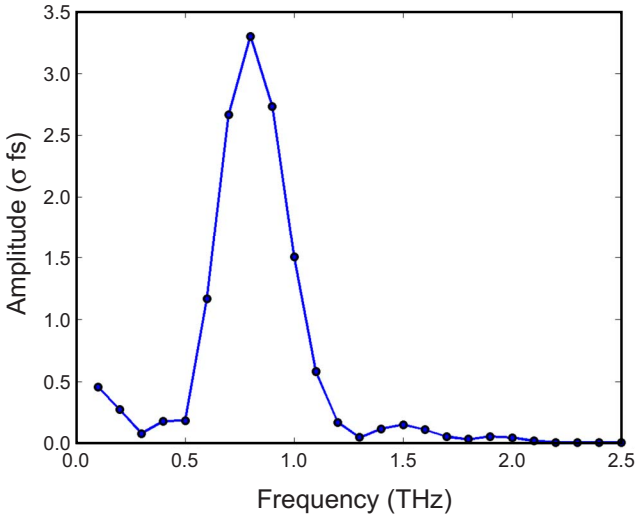


FIG. 5. (Color online) Corresponding frequency-amplitude spectrum of wave packet.

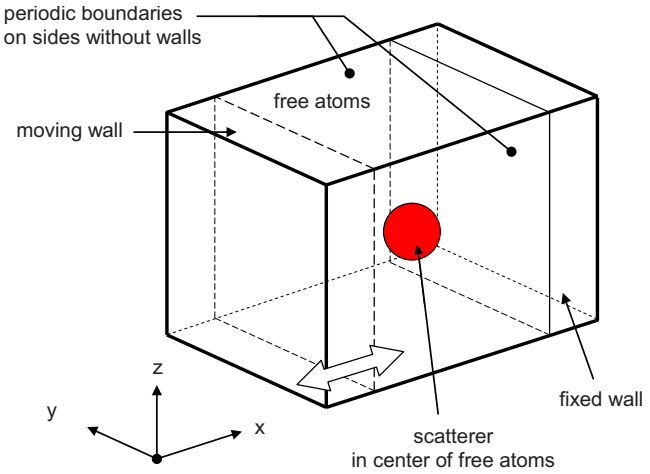


FIG. 6. (Color online) Arrangement of computational domain.

initial-condition-based approach uses fixed wall positions and imposes a wave packet in the domain upstream of the scatterer by assigning initial velocities and displacements to the atoms in order to form a traveling plane wave packet. Due to improved packet quality, this method is preferred over the method using boundary conditions. The simulations performed thus far all align the incoming wave's group velocity vector with the crystal's [100] direction, though the method using initial conditions is feasible and valid for any incident wave orientation and polarization, as are the postprocessing methods.

Primary outputs of the simulation are velocity vector and stress tensor data at multiple locations in space at multiple locations in time. The program calculates atomic-level stresses based on the equations of Vitek and Egami.[35] As necessary, it performs inverse-distance-weighted interpolation of the stresses at local atomic locations to get pressure at an arbitrary spatial location within the domain. These large arrays are postprocessed to calculate scattering information. Output data are sampled at a time resolution between 1 fs (the MD step size) and 10 fs to remain within memory limits during postprocessing. Simulated time ranges are typically in the range of 10 000–45 000 fs. The spatial resolution of the

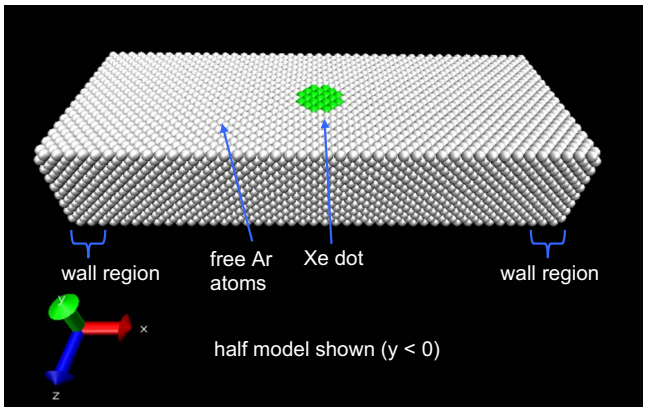


FIG. 7. (Color online) MD model section cut showing the position of Xe scatterer in Ar lattice.

points at which velocity and stress data are recorded may vary, with values of spacing typically $2.25° \leqslant \theta_{\text{spacing}} \leqslant 5°$ and $4.5° \leqslant \phi_{\text{spacing}} \leqslant 9°$.

## IV. METHOD FOR CALCULATING THE ORIENTATION OF VIBRATIONAL MODES

As part of the modeling process, it is necessary to identify the directions of oscillation associated with each of the vibrational modes. For each choice of wave vector **k** describing a wave propagating in a direction $(\theta, \phi)$, there are up to three distinct acoustic modes with orthogonal directions of oscillation. Along selected crystal axes, these may be pure modes (transverse and longitudinal) where the directions of atomic displacement are aligned perpendicular or parallel to the group velocity. In general, for an arbitrary choice of $(\theta, \phi)$, the modes are mixed (not pure) and must be determined by calculation. We use the following procedure, which is based on those described by Auld[36] and Carcione[37] for a continuous medium. An alternative to this method would be to perform the eigenvector calculations using a lattice dynamics model, an accurate but more complicated approach.

To begin, a strain tensor $\underline{\underline{S}}$ is defined as the (symmetric) gradient of the displacement vector $u_i$,

$$\underline{\underline{S}} = \frac{1}{2}(\nabla\vec{u} + \{\nabla\vec{u}\}^T) = \frac{1}{2}\left(\frac{\partial u_i}{\partial x_j} + \frac{\partial u_j}{\partial x_i}\right) = S_{ij}, \tag{4}$$

which is written as a six-element matrix $S_J^T = [S_{xx}\ S_{yy}\ S_{zz}\ 2S_{xy}\ 2S_{xz}\ 2S_{yz}]$. In a similar manner, the conventional symmetric stress tensor

$$\underline{\underline{T}} = \begin{bmatrix} T_{xx} & T_{xy} & T_{xz} \\ T_{xy} & T_{yy} & T_{yz} \\ T_{xz} & T_{yz} & T_{zz} \end{bmatrix} \tag{5}$$

is written as a stress matrix $T_I^T = [T_{xx}\ T_{yy}\ T_{zz}\ T_{xy}\ T_{xz}\ T_{yz}]$. The two are then related by the matrix equation $T_I = C_{IJ} S_J$, in which $C_{IJ}$ is a stiffness matrix. For a material with cubic crystal symmetries, $C_{IJ}$ will take the form

$$C_{IJ} = \begin{bmatrix} C_{11} & C_{12} & C_{12} & 0 & 0 & 0 \\ C_{12} & C_{11} & C_{12} & 0 & 0 & 0 \\ C_{12} & C_{12} & C_{11} & 0 & 0 & 0 \\ 0 & 0 & 0 & C_{44} & 0 & 0 \\ 0 & 0 & 0 & 0 & C_{44} & 0 \\ 0 & 0 & 0 & 0 & 0 & C_{44} \end{bmatrix} = \underline{\underline{C}}. \tag{6}$$

In this study, using 12-6 argon potentials, the values of the components are set to $C_{11} = 3.71 \times 10^{10}$ dyn/cm$^2$, $C_{12} = 2.07 \times 10^{10}$ dyn/cm$^2$, and $C_{44} = 2.15 \times 10^{10}$ dyn/cm$^2$, as documented by Barker *et al.* for 12-6 fcc argon.[38] For purposes of calculating normalized eigenvectors, the critical tasks are to select the proper form for $C_{IJ}$ and to establish the relative magnitudes (ratios) of the stiffness values.

Traveling wave motion is assumed, with wave number $k$, frequency $\omega$, and mass density $\rho$. For each direction of interest, the corresponding spherical coordinates $(\theta, \phi)$ are selected and used to generate a unit direction vector $\hat{l}$ in Cartesian coordinates,

$$\hat{l} = l_x\hat{x} + l_y\hat{y} + l_z\hat{z}. \tag{7}$$

The vector $\hat{l}$ is the direction of wave propagation and is aligned with **k**, which is not necessarily aligned with the local particle velocity or the group velocity vector. The group velocity vector $\mathbf{v}_g$ corresponds to the direction in which energy travels and is often called the energy propagation velocity $V_e$.

The vector $\hat{l}$ is used to define a matrix $\underline{\underline{L}}$,

$$\underline{\underline{L}} = \begin{bmatrix} l_x & 0 & 0 & 0 & l_z & l_y \\ 0 & l_y & 0 & l_z & 0 & l_x \\ 0 & 0 & l_z & l_y & l_x & 0 \end{bmatrix}. \tag{8}$$

For wavelike disturbances of the form $e^{i(kx-\omega t)}$, $-ik\underline{\underline{L}}$ will function as a spatial gradient operator. The motion of elastic waves is governed by the Christoffel equation, a three-dimensional form of the wave equation for linear elasticity in solids,[36,37,39]

$$k^2(\underline{\underline{L}} \cdot \underline{\underline{C}} \cdot \underline{\underline{L}}^T) \cdot \vec{u} = \rho\omega^2\vec{u}. \tag{9}$$

This eigensystem equation has up to three distinct eigenvalues and eigenvectors. The eigenvalues may be expressed as individual values of $\rho\omega^2/k^2$. The matching eigenvectors are the individual directions of oscillation of each mode. These eigenvectors are expressed as unit vectors and, for a wave propagation direction $\hat{l}$, may be ordered by increasing slowness (decreasing phase velocity) to define quasilongitudinal, quasifast transverse, and quasislow transverse modes in the linear regime. The wave vectors are mapped to group velocity vectors using Eqs. (10) and (11),[36]

$$\Omega = \det[k^2(\underline{\underline{L}} \cdot \underline{\underline{C}} \cdot \underline{\underline{L}}^T) - \rho\omega^2\underline{\underline{I}}], \tag{10}$$

$$v_{g\,i} = -\frac{1}{k}\frac{\partial\Omega/\partial l_i}{\partial\Omega/\partial\omega}. \tag{11}$$

With a chosen wave vector, to get a unit vector aligned with a group velocity, one need only calculate the numerator of Eq. (11) for three coordinate directions, generating Cartesian vector components proportional to those of $\mathbf{v}_g$, and then scale the vector to unit length. The sets of eigenvectors, wave vector, and group velocity vector are computed and tabulated for an array of $\theta$ and $\phi$ values.

## V. CALCULATION OF SCATTERING PHASE FUNCTIONS AND CROSS SECTIONS

The postprocessing method is based on the superposition of solutions for wave motion in a linear elastic solid. For small displacements, i.e., low temperatures, the crystal is expected to behave as a linear elastic material. In such a case, the incident wave packet and reflected wave packet are simply superposed. The form of the scattered wave packet is found by comparing the results of two separate molecular dynamics models, with and without the scatterer. The veloc-

ity vectors and stress tensors at chosen locations in space ($\vec{r}$ in spherical coordinates) are tracked over time for the two cases. Values of $\vec{r}$ are selected to cover the $(\theta,\phi)$ angular range of interest. The number of points selected determines the resolution of $\Phi(\theta,\phi)$. We typically use 100–300 values of $\vec{r}$, though a greater number will improve $\Phi$ resolution. In addition, spatial symmetries common to the crystal structure, simulation cell, and scatterer may be used to reduce the monitored range of $\phi$.

The relative differences between the two sets of results are defined as $\Delta\vec{v}=\vec{v}_{scatterer}-\vec{v}_{no\ scatterer}$ and $\Delta\underline{\underline{T}}=\underline{\underline{T}}_{scatterer}-\underline{\underline{T}}_{no\ scatterer}$, where $\vec{v}$ is the atomic velocity vector and $\underline{\underline{T}}$ is the stress tensor. As with $\vec{v}$ and $\underline{\underline{T}}$, both $\Delta\vec{v}$ and $\Delta\underline{\underline{T}}$ are functions of position $\vec{r}$ and of time $t$, and are stored as large arrays. To capture a far-field solution, the radial distances at which data are collected ($r$) need to be large compared to the size of the scatterer, so the changes in the components of $\vec{v}$ and $\underline{\underline{T}}$ are relatively small, meaning $|\Delta\vec{v}|\ll|\vec{v}|$. In addition to the primary scattering event, this set of $\Delta\vec{v}$ and $\Delta\underline{\underline{T}}$ time histories also contains signals associated with echoes of periodic reflections and with the reflection from the far wall of the simulation cell. After examining the results, a time range is chosen to identify and isolate the signals associated with the first reflected pulse due to the scattering event. This need to distinguish between the primary scattered signal, wall-reflected packet, and periodic echo signals puts a minimum size requirement on the simulation cell. For this method to work, it is necessary to clearly distinguish between the different signals by the time range over which they travel through the selected locations in space.

We then need a method by which we can use velocity, stress, and energy information to calculate heat flux. Following the heat flux equation of Volz and Chen[40], we can define an instantaneous heat flux at the location of an atom $i$. For pair potentials, the heat flux vector takes the form

$$\vec{q}_i=\frac{1}{V_i}\left[\vec{v}_i(\mathrm{PE}_i+\mathrm{KE}_i)+\frac{1}{2}\sum_{j,all\ j\neq i}^{N}\vec{r}_{ij}(\vec{v}_i\cdot\vec{F}_{ij})\right], \quad (12)$$

where $V_i$ is the volume associated with a single atom, $v_i$ is the atomic velocity, $\mathrm{KE}_i$ is the atom's kinetic energy, $\mathrm{PE}_i$ is the atom's potential energy, $r_{ij}$ is the relative position vector between atom $i$ and neighbor $j$, and $F_{ij}$ is the two-body interaction force between $i$ and $j$ ($\vec{F}_{ij}$ is parallel to $\vec{r}_{ij}$). The heat flux has units of energy per unit time per unit area and is analogous to the intensity $\mathcal{I}$ in acoustics. The summation may be divided into three terms,

$$\vec{q}_i=\frac{1}{V_i}\left[\vec{v}_i\mathrm{PE}_i+\vec{v}_i\mathrm{KE}_i+\frac{1}{2}\sum_{\substack{j=1\\ j\neq i}}^{N}(\vec{v}_i\cdot\vec{F}_{ij})\vec{r}_{ij}\right], \quad (13)$$

where the first term tracks the rate of transport of potential energy by atomic motion, the second term provides the rate of transport of kinetic energy by atomic motion, and the third term provides the energy transport rate associated with the work done by interatomic or intermolecular forces $F_{ij}$.

For our case of traveling harmonic wave motion, the time integral of the first term will go to zero when integrated over a full cycle, as the potential energy varies in phase with displacement, and the displacement is 90° out of phase with the velocity. Selecting a location $x$, we get $u\propto\cos(kx\text{-}\omega t)$ and $v\propto\sin(kx\text{-}\omega t)$. We then have a harmonic potential energy expression of the form $\mathrm{PE}\propto\mathrm{PE}_0+\mathrm{PE}_1\cos^2(kx\text{-}\omega t)$, in which $\mathrm{PE}_0$ is the potential energy when $u=0$ and $\mathrm{PE}_1$ is the maximum potential energy increase associated with the traveling wave. As a result, the first term of the heat flux equation is proportional to $\sin(kx\text{-}\omega t)[\mathrm{PE}_0+\mathrm{PE}_1\cos^2(kx\text{-}\omega t)]$. For any meaningful choices of the constants $k$, $\mathrm{PE}_0$, and $\mathrm{PE}_1$, and a selected value of $x$, this term yields a value of zero when integrated over a time interval corresponding to a cycle of oscillation ($t=0$ to $t=2\pi\omega$). Likewise, the second term will be proportional to $\sin^3(kx\text{-}\omega t)$, which has a time integral of zero over a full cycle.

The combination of the second and third terms is proportional to the vector-tensor product of stress and atomic velocity. If we define the atomic stress tensor $\underline{\underline{T}}_i$ as

$$\underline{\underline{T}}_i=-\frac{1}{V_i}\left[m_i(\vec{v}_i\otimes\vec{v}_i)+\sum_{\substack{j=1\\ j\neq i}}^{N}(\vec{F}_{ij}\otimes\vec{r}_{ij})\right] \quad (14)$$

per Ref. 35, we can rearrange the heat flux equation in the simpler form

$$\vec{q}_i=\frac{1}{V_i}\left[\vec{v}_i\mathrm{PE}_i+\vec{v}_i\mathrm{KE}_i+\frac{1}{2}\sum_{\substack{j=1\\ j\neq i}}^{N}\vec{v}_i\cdot(\vec{F}_{ij}\otimes\vec{r}_{ij})\right]=\frac{\vec{v}_i\mathrm{PE}_i}{V_i}-\frac{\vec{v}_i\cdot\underline{\underline{T}}_i}{2}. \quad (15)$$

The term $-\vec{v}_i\cdot\underline{\underline{T}}_i/2$ resembles the acoustic Poynting vector used in studies of continuum acoustics, for which the potential energy term $\vec{v}_i\mathrm{PE}_i$ is not a factor.

From this, we conclude that for pure harmonic wave motion or with well-formed wave packets, the PE and KE contributions to $\vec{q}_i$ due to atomic motion are not significant. We also note that the instantaneous transport of energy $\vec{q}_i(\vec{r}_i,t)$ is linearly proportional to atomic-level stress and linearly proportional to atomic velocity, the same principle seen in continuum acoustic theory. For cases with small atomic displacements in a single crystal (e.g., less than 1% of a lattice constant), the $V_i$ term varies very little during the motion and may be approximated as a constant, $V_i=V_{system}/N$. Thus, after time integration of a harmonic wave, the important intermolecular force term remains, giving

$$\vec{Q}_i=\frac{1}{2V_i}\int_{\mathrm{time}}\sum_{\substack{j=1\\ j\neq i}}^{N}(\vec{v}_i\cdot\vec{F}_{ij})\vec{r}_{ij}dt, \quad (16)$$

where $\vec{Q}_i$ represents the time integral of heat flux $\vec{q}_i$. As a result, the heat flux contribution of each pair $i$ and $j$ will be along $\vec{r}_{ij}$, the direction vector connecting the two atoms, and proportional to the projection of the atomic velocity $\vec{v}_i$ in this direction. The prefactor $1/2V_i$ appears in both the numerator and denominator of our equations for phase function and

cross section, and thus cancels out of the final equations. As long as displacements are small, the value of the prefactor is not important. In our present calculations, we preserve this constant as well as all of the terms in the heat flux equation in order to verify our expectation that the PE and KE terms have minimal contributions to the time-integrated heat flux.

It is expected based on acoustic theories that at sufficiently large $r$, meaning $r \gg a_{dot}$, the scattered wave will carry energy in the radial direction, away from the scatterer. Though the wave vector may have various orientations, $\mathbf{v}_g$ and $\vec{Q}_i$ should be parallel to $\vec{r}$. This alignment is checked during postprocessing of the MD results as a verification of the fundamental physics of the scattering model and the associated computational procedure shown in Eqs. (15) and (16). First, the center of the scatterer is assigned a coordinate (0, 0, 0) and used as the origin. The coordinate system is aligned with the crystal's cubic axes, so the incident plane wave travels along the Cartesian direction $+x$, which corresponds to the $\theta=0°$ direction. Scattered waves travel radially outward from the scatterer to reach the selected positions $\vec{r}$. The heat flux vector associated with the scattered wave is computed by examining the change in velocity and stress resulting from the inclusion of a scatterer. At sufficiently large $|\vec{r}|$, corresponding to a far-field location, we may state that in our lossless medium the group velocity is in the radial direction and then simplify the calculation procedure by setting $\vec{q}_{scattered}$ in the direction of $\vec{r}$. Our use of a wave packet to describe the motion of a particlelike phonon will occasionally cause the incident and scattered waves to overlap at various positions and times. This occurs when data are collected at a value of $r$ less than half the packet length. If terms of the type $\Delta\vec{v}\cdot\underline{\underline{T}}$ or $\vec{v}\cdot\Delta\underline{\underline{T}}$ are included in the heat flux equation, we will then be combining the incident and scattered wave effects and calculating "interference power," which is not the heat flux of the scattered wave. Incorporating these interference terms may result in scattered heat flux vectors that are not aligned with the radial unit vector, an indication of the error of such an approach. Following the approach of Gubernatis *et al.*,[41] we calculate $\Delta\vec{v}$ and $\Delta\underline{\underline{T}}$ and use terms of the form $\Delta\vec{v}\cdot\Delta\underline{\underline{T}}$ to examine the rate at which energy is carried by the scattered wave alone. This method yields $\vec{q}_{scattered}$ vectors, which are properly aligned in the radial direction, and this alignment is checked as part of the computational procedure. The average angle cosines between $\vec{q}_{scattered}$ and $\vec{r}$ are in the range of 0.95–0.99 for cases with $r > 3a_{dot}$.

At each selected point in space at each instant in time, the orientation of the local atomic velocity vector is compared to the three eigenvectors associated with mechanical vibrations to establish the fraction of energy in each mode. For a given direction, these fractions are labeled $F_1$, $F_2$, and $F_3$. These values are functions of $\theta$, $\phi$, and $t$ and thus form a large array of data. By examining when the atomic velocities increase and decrease, the time corresponding to the end of the incoming packet's passage is identified. An integration is performed over this carefully selected time interval for each point $\vec{r}$ to get the scattered energy per unit area in a particular mode, referred to as $Q_{is}$,

$$Q_{is}(r,\theta,\phi,\text{mode}) = \int_{time} F_{mode}(\theta,\phi,t) \times |-\Delta\vec{v}(r,\theta,\phi,t)\cdot\Delta\underline{\underline{T}}(r,\theta,\phi,t)/2|dt \tag{17}$$

or, more simply,

$$Q_{is}(\text{mode}) = \int_{time} F_{mode}|-\Delta\vec{v}\cdot\Delta\underline{\underline{T}}/2|dt, \tag{18}$$

noting that the PE term should not make a contribution. Here, the term $Q_{is}$ is tracked as a scalar because scattered waves are assumed to travel radially away from the scattering center at large $r$, but $\vec{Q}_{is}$ may be preserved as a vector if desired. It is commonly assumed that scattered wave power per unit area decreases in magnitude in proportion to $1/r^2$, the expected trend for a wave expanding from a pointlike scattering source, where $r$ is large compared to the length scale of the scatterer.[31] An examination of computed results collected at multiple radial distances in the model domain confirms that the $Q_{is} \propto 1/r^2$ trend is valid. At large $r$, meaning $r > 10a_{dot}$, the signal may become weak. To maintain a high signal-to-noise level, it is preferable to keep $r$ small. The desire to avoid collection of data in the near-field region motivates the selection of large $r$ values. In practice, our most successful models used monitoring points in the range $3a_{dot} < r < 10a_{dot}$. Our present model is constructed to collect data at points on a surface of constant $r$, though this is not strictly necessary.

Plotting $\Phi'(\theta,\phi,\text{mode}) = Q_{is}(r,\theta,\phi,\text{mode})r^2$ as a function of direction $(\theta,\phi)$ produces a phase function. $\Phi'$ is normalized to produce the phase function $\Phi$ based on the equation

$$\Phi(\theta,\phi,\text{mode}) = \frac{Q_{is}(r,\theta,\phi,\text{mode})r^2}{\frac{1}{4\pi}\int_{\phi=0}^{\phi=2\pi}\int_{\theta=0}^{\theta=\pi} Q_{is}(r,\theta,\phi,\text{mode})r^2 \sin\theta d\theta d\phi}. \tag{19}$$

Integration over the entire $4\pi$ steradians of solid angle $\varpi$ yields $\int_{\varpi}\Phi d\varpi = 4\pi$, and $\Phi$ may be interpreted as proportional to the probability density per unit of solid angle. This is similar to the procedure used for scattering of electromagnetic radiation.[42] The inclusion of the $r^2$ term in the equation allows for the possibility of collecting data at points with various values of $r$. With data sets collected at constant $r$, the $r^2$ terms cancel out of Eq. (19). A convenient feature of this method is that as long as all of the units used in the MD model are consistent, $\Phi$ will be normalized and dimensionless.

To obtain cross section $\Sigma_s$, a point in space is selected in a model without a scatterer. The value of $\vec{q}$ at this location is monitored to get an energy flux time history that describes the incoming packet. It is then integrated over time to get total incident energy per unit area passing through the do-

main in the unscattered packet, which is here labeled $Q_{incident}$. Total scattered energy $E_{scattered}$ is computed by integration,

$$E_{scattered}(\text{mode}) = \int_{\phi=0}^{\phi=2\pi} \int_{\theta=0}^{\theta=\pi} Q_{is}(r,\theta,\phi,\text{mode})\, r^2 \sin\theta d\theta d\phi. \tag{20}$$

While the time-integrated $Q_{is}$ is chosen to have units of energy per unit area, the integrated value $E_{scattered}$ has units of energy. The ratio of the total scattered energy to incident energy per unit area is a cross section $\Sigma_s$,

$$\Sigma_{s,\text{mode}} = \frac{E_{scattered}(\text{mode})}{Q_{incident}}, \tag{21}$$

which has the fundamental units of area used in the MD model ($\sigma^2$). A separate cross section is computed for each mode, and the sum of these gives the total cross section $\Sigma_s$. Dividing the value of $\Sigma_s$ by the scatterer projected area gives the scattering efficiency $C$ (where $C=\Sigma_s/\pi a_{dot}^2$ for a sphere). For a selected scatterer shape with a characteristic dimension $a_{dot}$, the use of $\Phi$ and $C$ allows description of scattering in completely nondimensional units.

We examine packet characteristics using the Fourier analysis of displacement data $\boldsymbol{u}(\boldsymbol{r})$ along radial lines (rays) starting at the origin (0,0,0) and extending in selected directions $(\theta,\phi)$ at a selected time $t$. Along axes of crystal symmetry, this produces a wave number–amplitude plot. From this, we confirm desired wave number components for particular directions of displacement (e.g., $x$ longitudinal, $y$ transverse, and $z$ transverse along the [100] direction). Selecting an early simulation time to capture $\boldsymbol{u}(\boldsymbol{r})$ gives wave number data for the incoming wave packet. Performing the Fourier analysis on $\boldsymbol{u}(\boldsymbol{r})$ at a suitably late simulation time gives wave number data for the scattered wave packet. We also use Fourier analysis with stress and pressure signals at selected points in space to get wave number–amplitude plots for the wave packets. This permits the use of model output to check the properties of the generated wave packet and show its composition in terms of frequency and wave number component(s).

## VI. RESULTS AND DISCUSSION

### A. Comparison to acoustic theory phase functions

The computational technique described above generates phase functions and cross sections for a variety of cases involving different scatterer shapes and sizes, different incident wave numbers and modes, and different scatterer atoms (rigid Ar and nonrigid Xe). The MD results for the rigid spherical scatterers are compared to the predictions of acoustic scattering theory, which was documented by Ying and Truell[30] for the case of a plane wave in an isotropically elastic solid with more than one permissible acoustic mode. If only longitudinal modes are present, the simpler case of theoretical fluid acoustics is applicable, and the same results are

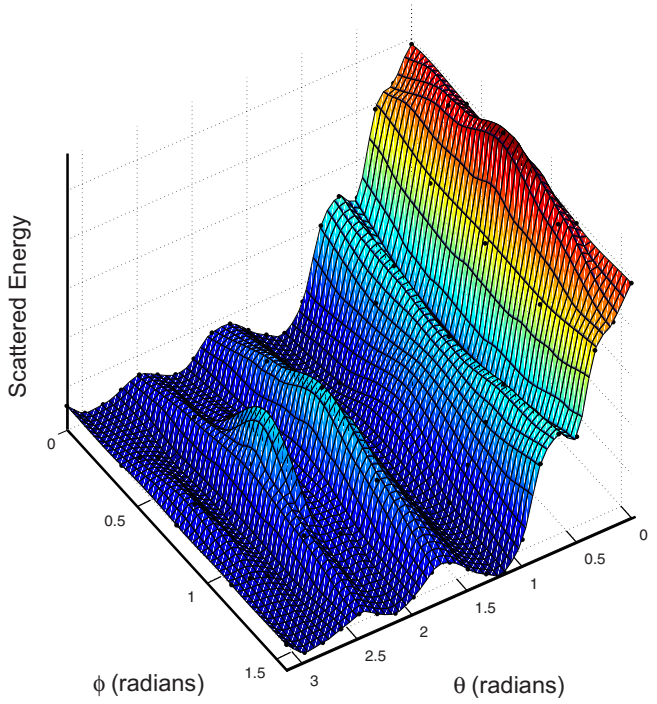


FIG. 8. (Color online) Example of full phase function, $k=1/\sigma$, $a_{dot}=3\sigma$, all modes.

obtained using the equivalent tabulated phase function data from Morse and Ingard.[31] In the acoustic theory, a scatterer has a phase function which is only a function of $\theta$, as the isotropy renders the problem completely symmetric with any rotation of angle $\phi$. This is not the case for scattering of an acoustic wave in an anisotropic crystal lattice, and $\Phi$ is expected to be a function of both $\theta$ and $\phi$. Figure 8 shows a phase function versus both $\theta$ and $\phi$. It is important to note that the function is not uniform with $\phi$, but has a larger sensitivity to changes in $\theta$ than to changes in $\phi$. For purposes of display and to ease comparison between different cases or configurations, many of the charts presented here use a $\phi$-averaged phase function $\Phi(\theta)$, which allows presentation in the polar plot format that is conventional in studies of radiation and acoustics. The simplified $\Phi(\theta)$ polar plot is useful as it gives a more intuitive picture of the relative numbers of phonons scattered in each direction. The two-dimensional depictions of $\Phi(\theta)$ shown herein are aligned with the direction of forward scattering ($\theta=0°$) to the right.

A sample comparison of $\phi$-averaged normalized phase functions for incoming longitudinal waves is shown in Fig. 9. In the majority of cases, the scattering phase function calculated from MD has features different from those of the acoustic theory prediction, which is based on an isotropic medium. The $\phi$-averaged MD results tend to have sharper lobes and may exhibit a greater number of small lobes, and the smaller lobes are shifted. The cases used in this study set the incoming wave vector along the [100] direction, which for small scatterers tends to cause narrow lobes (spikes) to form along the $\theta=0°$ and $\theta=180°$ directions, and decreases the amount of scattering in the lateral $\theta=90°$ direction. As scatterer size $a_{dot}$ increases with $A_{cell}$ and $ka_{dot}$ held fixed, the longitudinal-mode phase functions more closely resemble

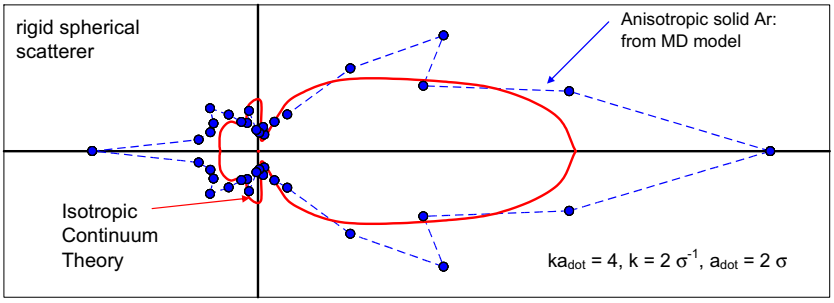


FIG. 9. (Color online) Phase function comparison for longitudinal mode, rigid spherical scatterer, $ka_{dot}=4$.

those of the acoustic theory, though some differences remain in the magnitude and positions of the smaller lobes. This is examined in greater detail in Sec. VI F. Due to multiple effects such as differences in scatterer shape and roughness and anisotropy of the crystal's elastic properties, the physical phenomena captured in acoustic theory and MD are not identical, and these are believed to be the reasons for the observed differences, as discussed in Sec. VI B.

The equation set of Ying and Truell clearly separates the longitudinal and transverse components of the scattering amplitudes. This allows us to compare the theoretical and the computed results for scattering into the transverse mode in the anisotropic solid. Due to the anisotropy, there are separate quasifast transverse and quasislow transverse modes. By summing the energies in these two modes, we can produce a $\phi$-averaged phase function for scattering into all quasi-transverse modes, an example of which is shown in Fig. 10. This phase function can be compared to the analytical prediction of Ying and Truell seen in the same figure. Both functions show the expected nulls at 0° and 180°. They also have strong sideward and forward lobes, but the lobes generated by the anisotropic MD model have shifted and, after $\phi$ averaging, show reductions around 35° and 125°. The sin $\theta$ term necessary in the spherical coordinate integration causes the normalization to exaggerate the differences in the analytical and MD-calculated lobes. This trend of an anisotropic scattering medium giving a phase function with shifted lobes and sharp local decreases is also seen in the computational work of Temple.[28]

### B. Causes of variation between theoretical and computed phase functions

This initial comparison between the theoretical isotropic fluid acoustic phase functions and the molecular dynamics results highlights a number of important differences between the two.

(1) The acoustic theory presented by Morse describes wave motion in an isotropic material. The solid argon fcc structure is not isotropic but instead has stiffness that varies with direction, which results in increases and decreases in $\Phi$ along certain directions when compared to $\Phi$ for an isotropic material. This effect will persist at all length scales within a crystal and is a dominant effect, which is infrequently discussed in the literature covering scattering of phonons. We separately used this model to simulate propagation of waves from a point source in a crystal,[34,43] and these phonon imaging results compared favorably with those of phonon focusing experiments,[44] indicating that the model properly accounts for the influence of anisotropy on group velocity.

(2) The continuum theory of acoustics has mass distributed uniformly through space. The solid argon structure has mass associated with discrete atoms, which results in a dispersion curve. The majority of models used in this study have low wave numbers for which the dispersion relation $\omega$ vs $k$ is close to linear, though wave speed is still a function of the direction of $\mathbf{k}$. The molecular dynamics model accounts for dispersion at all values of $kA_{cell}$ and can also properly model wave motions in the continuum regime ($kA_{cell} \ll 1$).

(3) Due to the discrete nature of the lattice, the scatterer shape used is granular and has a lumpy or faceted surface, instead of the spherical surface of the continuum theory. For large scatterer sizes ($a_{dot} > 10A_{cell}$), this effect becomes less significant. The continuum description identifies a scatterer boundary at a precise location in space, while in the simulation the boundary between free and rigid atoms spans a finite region. In addition to the aspherical surface, the prepositioning of the atoms within and adjacent to the scatterer restricts the force interactions to a finite number along particular axes, though atomic displacements can, in principle, occur in any direction. Compared to the continuum theory, the granular lattice of discrete masses has fundamental differences in both the nature of the scatterer and its mechanical interactions with the wave packet.

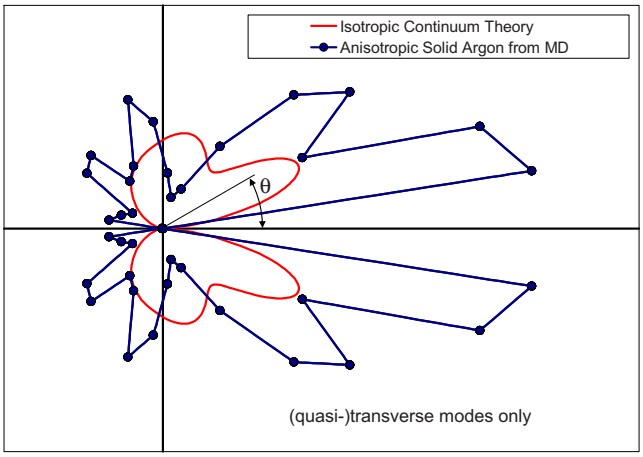


FIG. 10. (Color online) Phase function for the sum of quasi-transverse modes, analytical equations of Ying and Truell vs anisotropic MD model, longitudinal incoming wave, $ka_{dot}=3$, $k=1/\sigma$, $a_{dot}=3\sigma$.

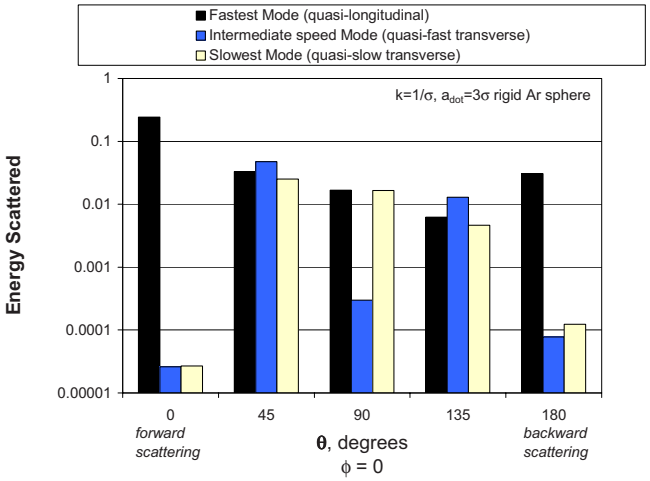


FIG. 11. (Color online) Scattered energy per unit area vs direction, longitudinal incoming wave, $k=1/\sigma$, $ka_{dot}=3$, nondimensional (relative) scale.

(4) The propagation of waves in the argon is not purely harmonic. All force interactions are slightly nonlinear, with the spring constant becoming progressively more nonlinear with larger deflections. This causes some unavoidable degradation of packet shape, which can be limited by using low-intensity wave packets (maximum displacement $<A_{cell}/100$).

(5) The incoming wave packet is not and cannot be at an exact value of $k$, but has a range in its component values of $k$ and $\omega$. Lengthening of the packet decreases its lateral span on the amplitude–wave number charts.

(6) The solutions found in the continuum theory describe scattered energy distributions in the far-field region, where $r$ approaches $\infty$. The solutions generated by the MD model certainly cannot reach $r=\infty$; instead, the model uses $r$ values one order of magnitude greater than $a_{dot}$. Further increasing $r$ steeply increases the computational cost due to the necessary increase in simulation cell extent, and for larger $r$, postprocessing may reveal an insufficient signal-to-noise ratio. As a result, the MD solutions are not completely far-field solutions but have unavoidable traces of near-field solution patterns.

Of these differences, the first and third have the greatest influence on the phase functions examined herein. The second difference is minor for values of $k$ less than 30% of $k_{max[100]}$, and the fourth difference is reduced by selecting small displacements. The first three differences are based on the physical behavior of materials, while items (4)–(6) result from modeling limitations.

### C. Energy present in each mode

The intensity of the various modes may be compared, as shown in Fig. 11, which presents the relative energy per unit area scattered from a longitudinal incoming plane wave by a rigid spherical inclusion. The presence of additional modes with nonzero energy confirms that mode conversion occurred as part of the scattering event. Here, the assignment of labels qL, qFT, and qST is conducted by independently evaluating the speed of each mode at each individual direction selected. It is visible that in the forward and backward directions the scattering of energy is primarily in the quasilongitudinal mode, as expected based on the acoustic theory. The presence of a large longitudinal component near the $\theta=90°$ side sector is the result of a particular choice of $ka_{dot}$, and small changes in $ka_{dot}$ may make large shifts in the alignment of this lobe, a characteristic also seen in acoustic theory. The total amount of energy in each mode, when properly summed (area weighted), gives the relative probability of scattering into each mode. The relative height of the bars gives the relative probability of scattering into each direction.

### D. Scatterer shape and roughness

For small dots with $a_{dot}<3A_{cell}$, the effects of scatterer granularity and limited directions of force interaction cause changes in $\Phi$. Though all of the nominally spherical dots are generated by selecting atoms within a well-defined spherical boundary, the actual surfaces of the small dots have lumps or facets rather than the smooth spherical boundary described in the continuum theory. Forces causing reflection events near the scatterer atoms are limited to discrete atomic interactions in preset directions, the stiffnesses of which vary with distance due to anharmonicity and vary with direction due to elastic anisotropy.

To see some of these effects, we compare cubic scatterers to the roughly spherical scatterers. Changes in $\Phi$ are seen as a result of the faceted shape of the cubic scatterer. Figure 12 shows an example of $\Phi$ for a case with a cube of side length of $6\sigma$, faces along the {100} planes, and packet wave number $1/\sigma$. The plot includes a comparable $\Phi$ for a spherical scatterer. Total phase functions are used, rather than separate modal phase functions (qL, qFT, and qST), to more clearly illustrate the proportion of energy traveling in each direction. The total phase function may be compiled by setting the factor $F_{mode}$ to a value of 1 in Eq. (17), simply integrating all scattered wave energy traveling through each monitoring point and normalizing per Eq. (19).

The cubic inclusion's $\Phi$ shape has a larger lobe in the backward region, aligned with its natural facet. The sideward-scattered lobes have decreased in size as well. This shows geometric-scattering characteristics that scatterers will start to exhibit as $ka_{dot}$ increases beyond 1, approaching the geometric regime of $ka_{dot}\gg 1$. It also indicates that controlling the shape and alignment of inclusions in a material may allow the designer to channel scattering along particular directions.

As actual nanometer-scale structures may not have clean, sharply defined boundaries, it is useful to consider the influence of additional roughness caused by less-than-perfect scatterer boundaries. This is simulated by rearranging the atoms near the surface of the scatterer and randomly selecting their type until a particular scatterer mass is reached. Figure 13 shows a randomly roughened spherical scatterer compared to a smoother spherical scatterer of the same mass, with $ka_{dot}=3$. The total phase function of the roughened scatterer has the same general shape with an increase in the size of the backscattered lobes. The roughening process used here effectively raises $a_{dot}$ while maintaining the same scatterer

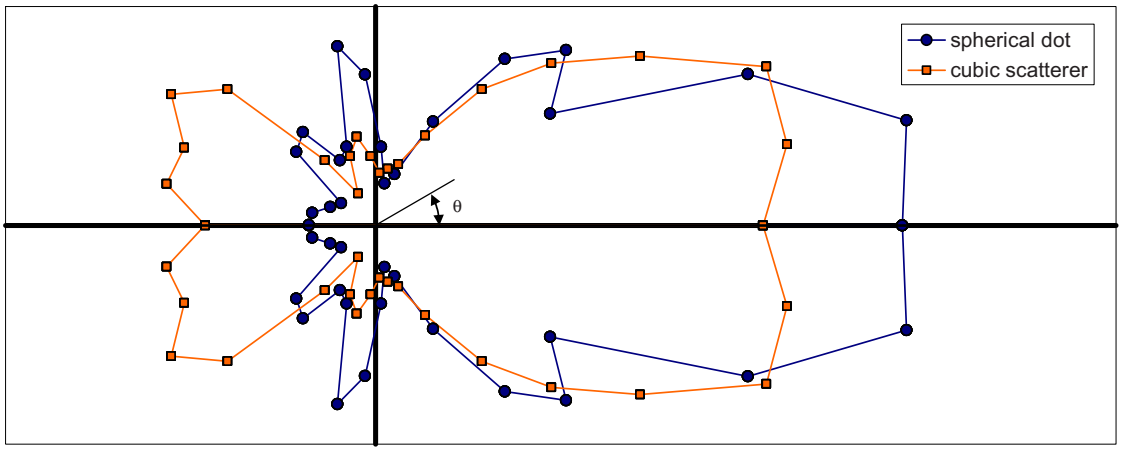


FIG. 12. (Color online) Total phase functions, cubic vs spherical scatterers, $ka_{dot}=3$, normalized.

mass. The increase in $ka_{dot}$ would decrease the size of the lobes for a case with a smooth scatterer. The change to a slightly rougher scatterer thus results in a scattering event which is more diffuse than that of the smooth scatterer with regular surfaces. Also visible in the phase function is a decrease in the direct backscatter lobe at $\theta=180°$ due to the removal of a backward-aligned scatterer facet upon roughening.

To investigate shapes similar to experimentally fabricated nanostructures,[14] models of pyramid-shaped scatterers were used. The resulting total phase functions shown in Fig. 14 correspond to cases with pyramids of height $3.5\sigma$ and base dimensions $7\sigma\times7\sigma$. The $ka_{dot}$ value of 3.5 used in this case suggests that the scattering will have a large geometric component. The phase function shows that at high $ka_{dot}$, the faceted nature of the scatterer has a strong influence. The incident wave is strongly reflected from the pyramid base and creates a large backscatter lobe. In the case with the wave incident on the pyramid apex, the phase function has side lobes not present in the case with the base incidence. The similarities between the base-incidence case and that of the cubic dot show that at higher $ka_{dot}$ values with a rigid scatterer, the incident wave is primarily influenced by the leading surface of the inclusion and weakly influenced by the rear surface, as seen with geometric scattering from a reflective object.

The difference between the two phase functions at high $ka_{dot}$ values indicates that the thermal conductivity can depend on direction in a fabricated solid structure containing pyramidal scatterers of controlled orientation (e.g., a Si-Ge quantum dot superlattice), rather than remaining invariant following a $\Delta\theta=180°$ rotation. As temperature increases, the phonon-phonon scattering events may overcome this inclusion-based method of controlling conductivity, but a weak directional dependence will remain for some range of phonon wave numbers. It is possible that at some combination of scatterer size and temperature, the dominant phonon wave number(s) will be high enough that heat conduction may have a strong dependence on material orientation, creating a material with diodelike properties only available through the use of nanometer-micrometer-scale structures.

### E. Mass, strain, and stiffness effects on scattering

To examine the effects on scattering of inclusions with different masses, stiffnesses, and lattice constants, six types of inclusions were investigated: (1) rigid argon, (2) an argon isotope with the mass of krypton (2.1 times that of argon),

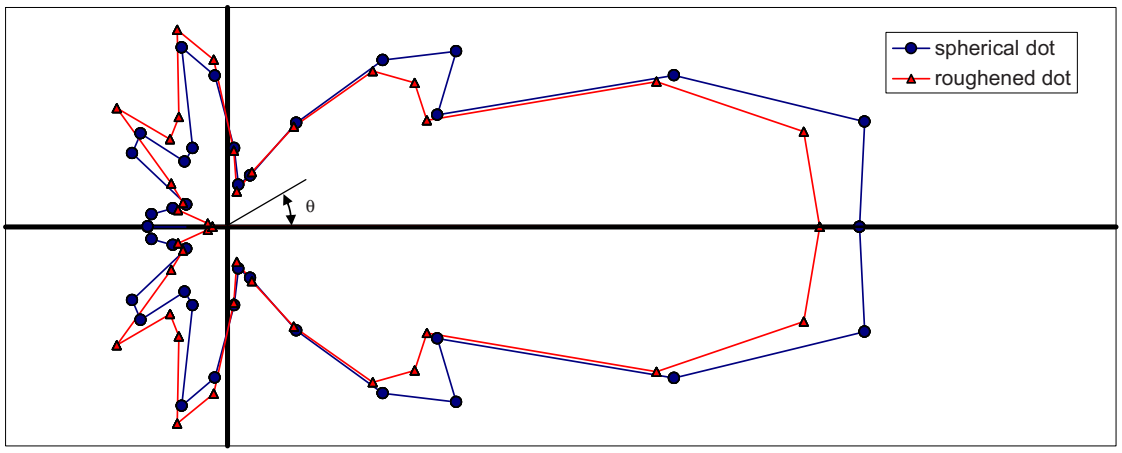


FIG. 13. (Color online) Phase functions, rough vs smooth spherical scatterers, $ka_{dot}=3$, normalized.

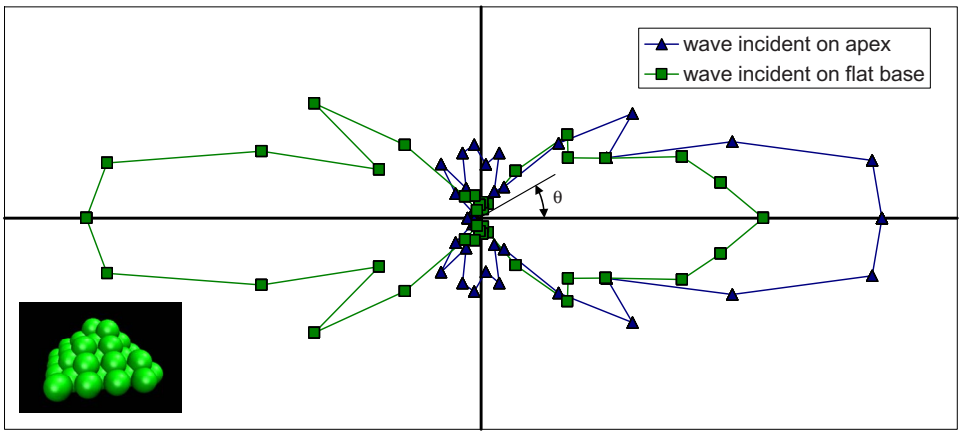


FIG. 14. (Color online) Total phase functions for rigid pyramid-shaped scatterers, wave incident on base and apex, $k=1/\sigma$, $7\sigma\times7\sigma\times3.5\sigma$ inclusion dimensions, normalized.

(3) an argon isotope with the mass of xenon (3.3 times that of argon), (4) a xenonlike material, but with the argon energy scale parameter $\varepsilon$, (5) xenon, and (6) an argon isotope with ten times the mass of argon. Table I gives the masses, Lennard-Jones energy parameters, and Lennard-Jones spacing parameters for the cases and also shows the resulting scattering cross sections. All of the cases are set at $k=1$ and $a_{dot}=2$, and the spherical inclusions are embedded in a lattice of mobile argon atoms. For these cases, the scatterer is very lumpy and granular, with $kA_{cell}=1.5$. The total scattering phase functions for these cases are shown in Figs. 15–17.

Figure 15 presents the effects of changing scatterer mass. It compares the phase functions for the cases with a completely immobile scatterer and three isotopes of argon. The phase functions are normalized, but we can see differences in the relative distribution of scattered energy. In general, increases in mass are accompanied by higher backscattering. The rigid argon phase function is very similar to that of the extremely high-mass inclusion ($m=10m_{\mathrm{Ar}}$, case 6), supporting the description of the rigid scatterer as one with effectively infinite mass. However, it should be mentioned that the rigid inclusion displays somewhat larger forward ($\theta=0$) scattering than the comparable high-mass inclusion of case 6. We believe that this arises from the additional effect of the infinite stiffness of the rigid particle. This belief is supported by a comparison to Fig. 17, which shows higher forward scattering for stiffer particles.

Figure 16 shows the effects of changing the inclusion lattice constant $\sigma$, which causes lattice strain. This causes a local change in elasticity that extends beyond the surface of the scatterer. In addition to strain in the argon, the exterior portions of the xenon dot are compressed by the argon. Both within the inclusion and in the strain-affected region adjacent to the inclusion, there are spatial variations in mass density, material stiffness, and the dispersion relations. Wave fronts passing through the strained region will bend slightly due to mild refraction. The change in local stiffness will also cause reflection of a small portion of the wave energy. In addition to changing the phase function due to redirection of the backscattered waves, this causes phase shifts in some portions of the forward-moving wave front, which do not directly contact the xenon atoms. Though primarily in the forward direction, these mild phase shifts come from interactions that are ultimately caused by the scatterer and are thus interpreted as legitimate scattering events. As a result, the influence of the dot extends beyond $a_{dot}$, increasing the scattering efficiency. A phase shift in forward-scattered waves with almost no bending of the wave front would appear as an increase in $\Sigma_s$ and a growth in the forward lobe of $\Phi(\theta\phi)$ which, taken together, would make very little change in the rate at which phonons travel through the medium. The local strain affects waves both before and after they reach the inclusion, resulting in a very different boundary condition compared to that of the rigid scatterer. For case 4, the lattice strain and the change in stiffness combine to increase the cross section by 50% as compared to case 3. The lobes in case 4, with the strained lattice, have rotated farther forward and the side lobes have grown as well, showing a strong redirection of energy by the inclusion with the larger lattice constant.

TABLE I. Scatterer characteristics and scattering cross sections for different inclusion cases.

| Case | Description | $\varepsilon/\varepsilon_{\mathrm{argon}}$ | $\sigma/\sigma_{\mathrm{argon}}$ | $\mathrm{Mass}/\mathrm{Mass}_{\mathrm{argon}}$ | $\Sigma_s$ |
|---|---|---|---|---|---|
| 1 | Rigid argon | 1 | 1 | effectively $\infty$ | 16 |
| 2 | Argon isotope, mass of Kr | 1 | 1 | 2.1 | 13 |
| 3 | Argon isotope, mass of Xe | 1 | 1 | 3.3 | 24 |
| 4 | Xenonlike with argon bond energy | 1 | 1.15 | 3.3 | 35 |
| 5 | Xenon | 1.92 | 1.15 | 3.3 | 55 |
| 6 | Argon isotope, ten times mass of Ar | 1 | 1 | 10 | 17 |

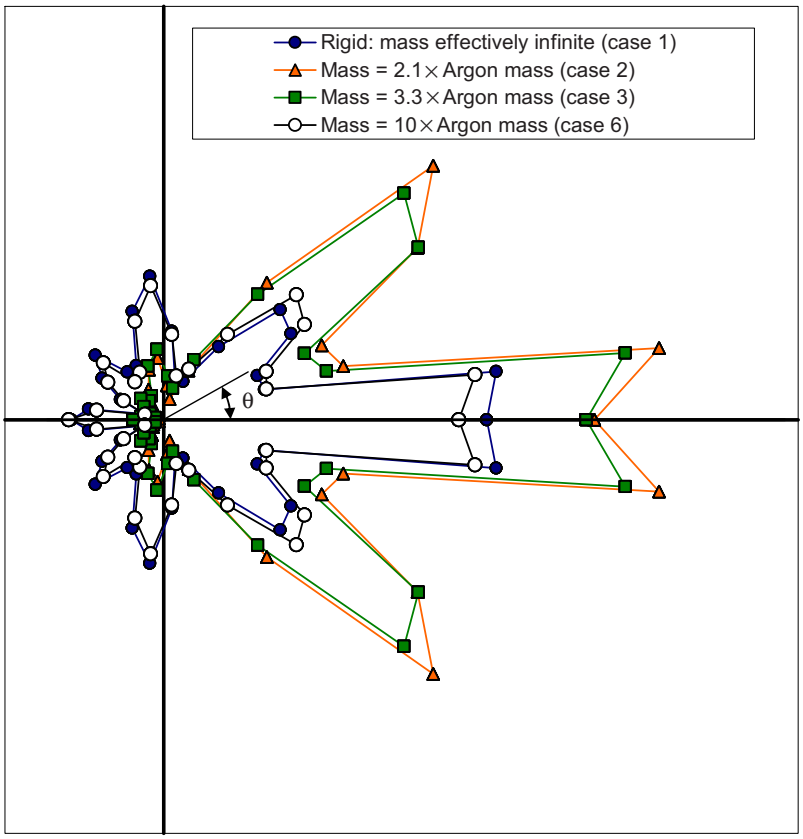


FIG. 15. (Color online) Total phase functions of argon isotopes, scattering from rigid and nonrigid inclusions, $ka_{dot}=2, \varepsilon=\varepsilon_{\mathrm{Ar}}, \sigma=\sigma_{\mathrm{Ar}}$.

Figure 17 shows the effects of a bond energy change for cases with the same mass and lattice constant. In these cases, both of the scatterers have atoms with the mass and lattice constant of xenon but different values of the binding energy constant $\varepsilon$, which results in different forces. Case 5 has a 92% stiffer bond, and this results in a 54% greater cross section. The increase is seen primarily as a growth in the forward-scattered lobe.

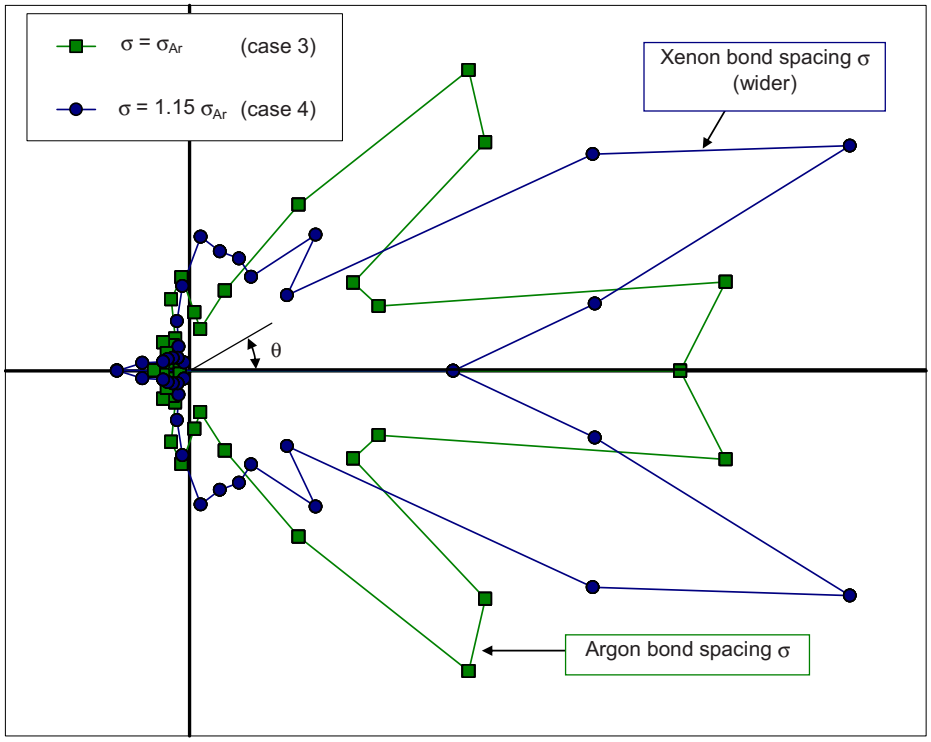


FIG. 16. (Color online) Total phase functions, scattering from inclusions of differing bond length, $ka_{dot}=2$, mass$=3.3m_{\mathrm{Ar}}$, $\varepsilon=\varepsilon_{\mathrm{Ar}}$.

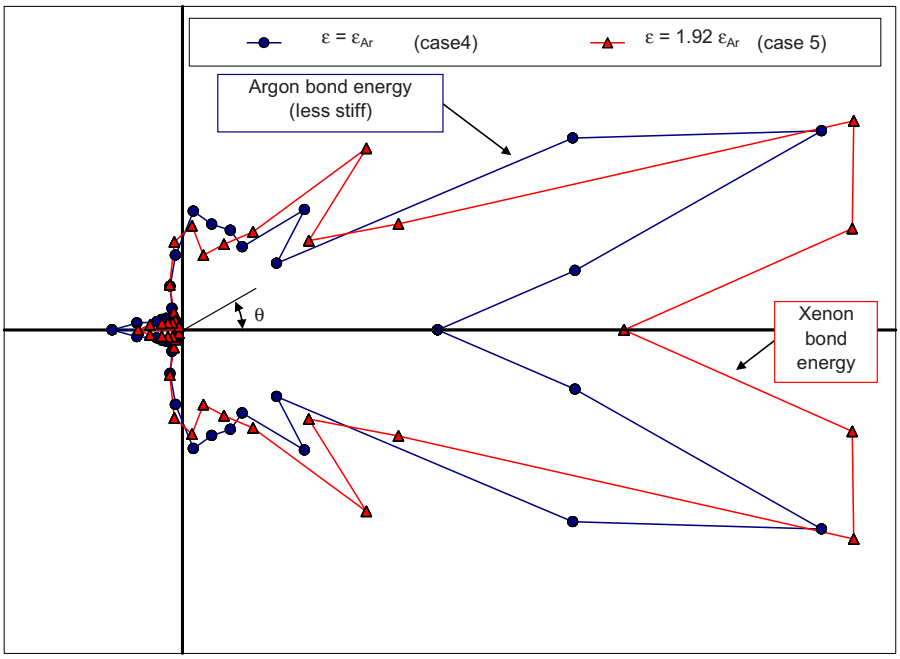


FIG. 17. (Color online) Total phase functions, scattering from inclusions of differing bond energy, $ka_{dot}=2$, mass$=3.3m_{\mathrm{Ar}}$, $\sigma=1.15\sigma_{\mathrm{Ar}}$.

In cases where the $\varepsilon$ and $\sigma$ parameters of the inclusion material differ from those of the host, atomic disordering occurs in the vicinity of the interface. To capture this effect, molecular statics calculations are performed to find a relaxed configuration of host and inclusion atoms for all cases except those with rigid inclusions. After reaching static equilibrium at 0 K, the argon lattice has a new nonuniform spacing in the vicinity of the inclusion, which becomes the initial condition of the molecular dynamics calculation. This variation in atomic spacing may also be described as a change in local number density, as shown in Fig. 18 for a spherical volume with a radius of $2\sigma$ surrounding each atom.

The strain-induced refraction effects add another requirement on the choice of $r$ at which data are collected. The value of $r$ needs to be well outside the strain-affected region, at least greater than $3a_{dot}$ and ideally as high as $10a_{dot}$. The suitability of a chosen value of $r$ at which data will be collected is evaluated by comparing the calculated strains associated with scattered waves with the initial local strain associated with the nearby inclusion atoms. This condition may be alternately described as a requirement for the difference between initial stress fields $T(\boldsymbol{r},t=0)$, with and without the scatterer, to start out at approximately the same values such that elements of $\Delta T$ are very small at time $t=0$, much smaller than the stresses generated by the incoming wave. This is achieved by selecting large $r$ and by using a large cubic simulation cell to reduce the irregularity of the strain field due to the different far-field boundaries. If the incoming pulse amplitude is too low, then the reflected signal (stress field) would be faint compared to that of the initial stress field.

### F. Scaling of results

The characteristic sizes of the quantum dots in quantum dot superlattices typically range from a few nanometers to tens of nanometers. The present MD method used to investigate scattering from nanometer-scale inclusions becomes prohibitively expensive for inclusion sizes larger than about 10 nm, so it is useful to investigate whether results calculated for small inclusion sizes ($<$10 nm) can be scaled to predict scattering cross sections and phase functions for much larger inclusions. In acoustic theory, which assumes perfectly sharp, smooth interfaces and specular reflections, the scattering cross sections and phase functions depend only on $ka_{dot}$ and do not specifically depend on inclusion size $a_{dot}$. This indicates that scattering of large wave number waves from small inclusions should be identical to scattering of small wave number waves from large inclusions, provided that $ka_{dot}$ is the same in both cases. In other words, scattering cross sections and phase functions for large inclusions could

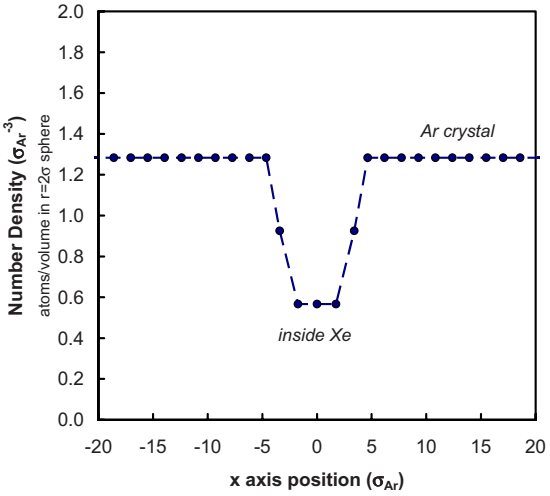


FIG. 18. (Color online) Local density profile due to mismatched inclusion particle (Xe in Ar).

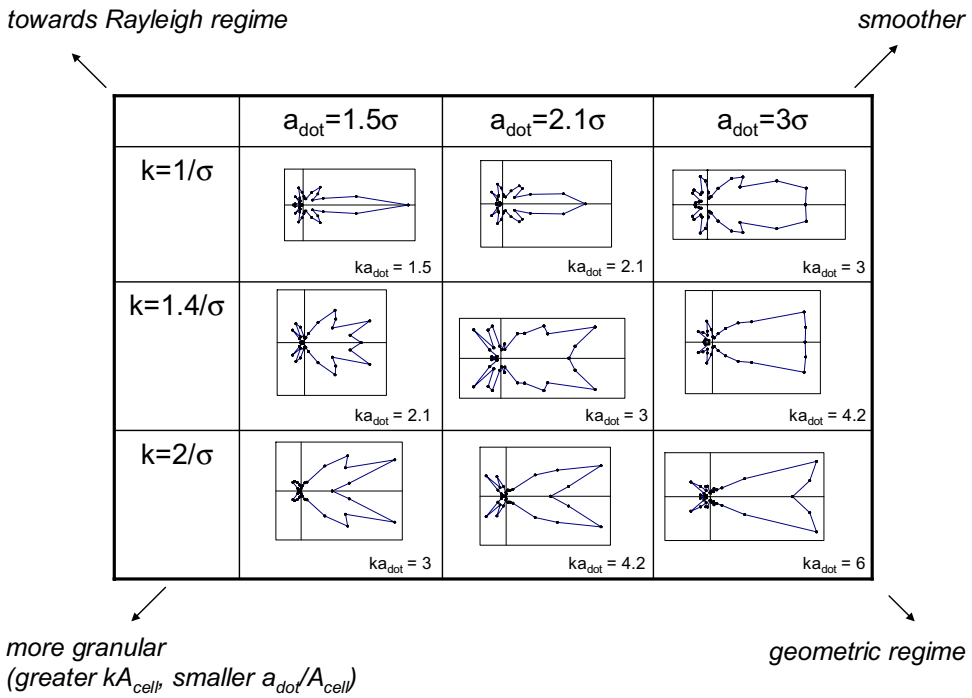


FIG. 19. (Color online) Total phase functions for rigid Ar spherical scatterers, longitudinal incoming wave, $A_{\mathrm{cell}}=1.55\sigma$.

ideally be predicted from simulation runs on much smaller systems, provided the wave numbers are scaled appropriately. Unfortunately, this is not always possible due to the influence of a second parameter that is important in realistic systems but neglected in acoustic theory: the roughness parameter $kA_{cell}$.

The roughness parameter measures the atomic granularity of the scatterer and is effectively a measure of the unavoidable surface roughness present with small inclusions. Small scatterers constructed to resemble spheres (e.g., Fig. 7) have facets due to the underlying crystal structure, and for higher wave numbers these facets direct energy in particular directions. At small $kA_{cell}$, the inclusion surface appears smooth to the incoming wave, scattering is specular, and acoustic theory applies. At large $kA_{cell}$, the inclusion surface appears rough to the incoming wave and scattering is diffuse. In addition, for small scatterers, the lattice granularity restricts strong force interactions near the scatterer surface to a finite number, generally along directions of close atomic packing. These directions of strong force interactions are fixed by the lattice and do not rotate with a change in incoming phonon direction $(\theta',\phi')$. These atomic-scale effects are, of course, not addressed in the continuum acoustic theory. The shifts in lobe patterns caused by material anisotropy should occur at all length scales.

A series of phase function calculations for various combinations of $k$ and $a_{dot}$ with $A_{cell}$ fixed were performed to determine how smooth the surface must be (how low $kA_{cell}$ must be) in order for scaling to be applicable. Figure 19 contains a table of the obtained phase functions. In this figure, the size and roughness parameters can be varied independently to isolate their respective effects on scattering. The size parameter can be increased while holding the roughness parameter constant by progressing left to right across the rows in the table. The roughness parameter may be increased while holding the size parameter constant by progressing from top right to bottom left along the diagonals in the table. The upper right corner of the table presents cases with the smoothest, most spherical dots, relative to packet wavelength. Isotropic acoustic theory predicts that for the range $2<ka_{dot}<10$, the total phase function for all modes should appear as a large forward lobe with a lesser scattering into the sideward and backward directions, the region spanning $45°<\theta<315°$. As the size parameter $ka_{dot}$ increases, the primary forward lobe should increase in radius, and the remainder of the phase function should decrease in radius. As this trend progresses, the number of lobes in a given mode's phase function may increase, while the they decrease in width and length. This is illustrated in Fig. 20 which presents the corresponding isotropic continuum phase functions for all modes (total $\Phi$) calculated per Ref. 30. The MD results show that as $ka_{dot}$ increases, the size of the forward-scattered lobe grows and the backscattered energy decreases, which follows the trend of the acoustic theory. This corresponds to a transition from the upper left corner to the lower right corner of Fig. 19.

The $k=2/\sigma$, $a_{dot}=1.5\sigma$ phase function serves as an extreme example of the changes in phase functions resulting from inclusions with a nanometer length scale. For this case in the lower left corner of Fig. 19, the phase function does not resemble that of the continuum theory due to the great differences in the scatterer shape and interaction mechanics at or near the scatterer surface. Moving diagonally across Fig. 19, from the lower left corner to the upper right corner, the dot surface becomes smoother and the phase function starts to take on the expected shape of a single forward lobe with smaller features in other directions. As none of the diagonal images of Fig. 19 with identical $ka_{dot}$ have matching

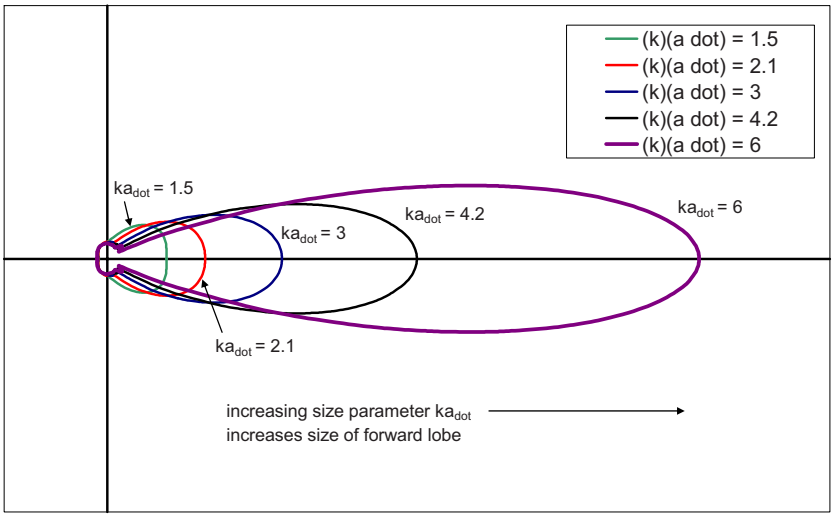


FIG. 20. (Color online) Continuum phase functions, total of all modes, $ka_{dot}$=1.5–6.

phase functions, we concluded that scaling could not yet be justified in this range of $kA_{cell}$. We further investigated configurations for which $ka_{dot}$=3 to look at trends for lower $kA_{cell}$ (lower roughness). Figure 21 shows additional phase functions for the $ka_{dot}$=3 case at progressively lower $k$, lower $kA_{cell}$, and greater $a_{dot}$. It also shows the normalized isotropic continuum theory phase function for all modes and the geometric-limit diffuse scattering theory phase function [Eq. 11–92 in Ref. 42]. The resulting trend running from large $kA_{cell}$ (very granular) to lower $kA_{cell}$ (smoother) is a decrease in the energy scattered to the side and back sectors and the development of a single large lobe in the forward direction, as expected for phase functions with $ka_{dot}>2$. This behavior is consistent with a transition from diffuse scattering at high $kA_{cell}$ to specular scattering at low $kA_{cell}$. The phase functions for larger $a_{dot}$ and smaller $k$ show forward lobe shapes and sizes closer to those found in the isotropic continuum theory. Even at very low $kA_{cell}$, the $\phi$-averaged phase functions are not identical to those of continuum theory due to material anisotropy.

To first order, the $ka_{dot}$=3 phase functions have the same general shape and local magnitudes for the cases with $k$=1, $a_{dot}$=3 and $k$=0.67, $a_{dot}$=4.5 (Fig. 21). This first-order similarity does not hold for cases with $kA_{cell}\geqslant 1.5$, here equivalent to $a_{dot}/A_{cell}<2$. Based on these computed results, results for cases with $ka_{dot}$ of order of magnitude 3 and $kA_{cell}\leqslant 1.5$ are expected to match to first order when scaled up to greater $a_{dot}$ at given $k$ and $A_{cell}$. As an attempt to simulate a 10 nm inclusion particle and collect far-field scattering data will require many millions of atoms and may thus be impractical,

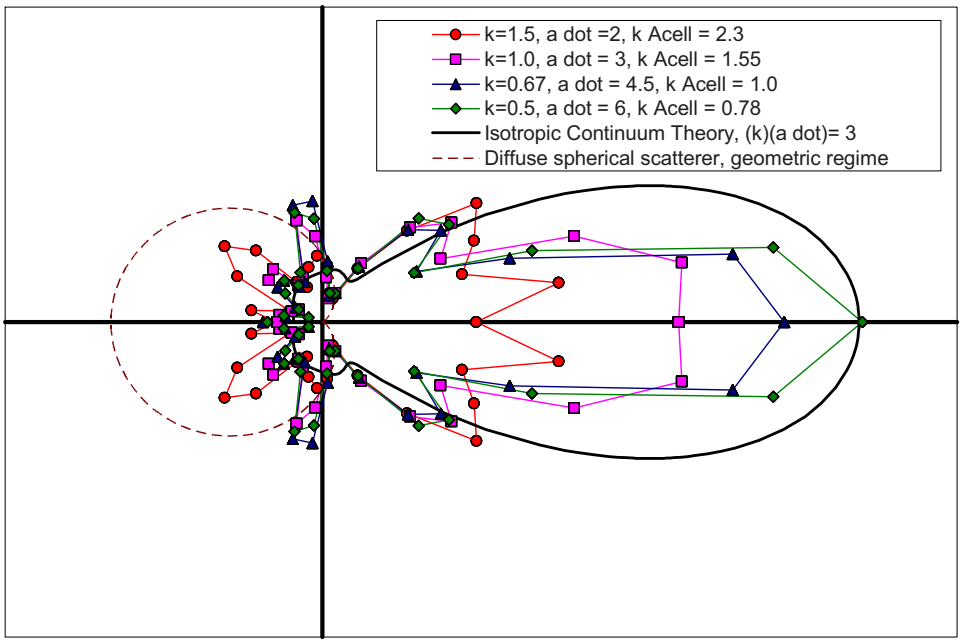


FIG. 21. (Color online) Total phase functions (all modes) for various scatterer length scales, $ka_{dot}$=3, rigid scatterer. The decrease in $kA_{cell}$ shows a transition from diffuse to a specular scattering behavior.

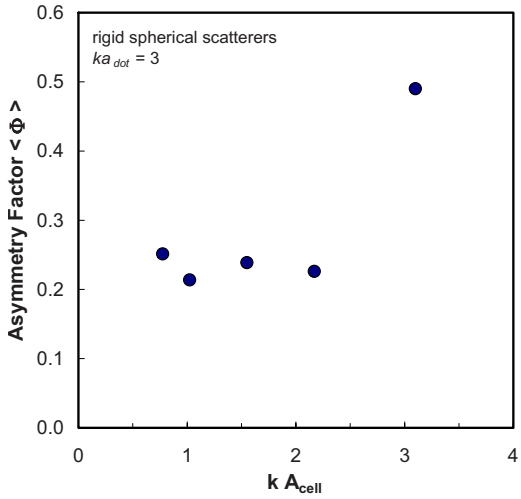


FIG. 22. (Color online) Asymmetry factor vs lattice granularity parameter $kA_{cell}$, rigid scatterers, $ka_{dot}=3$.

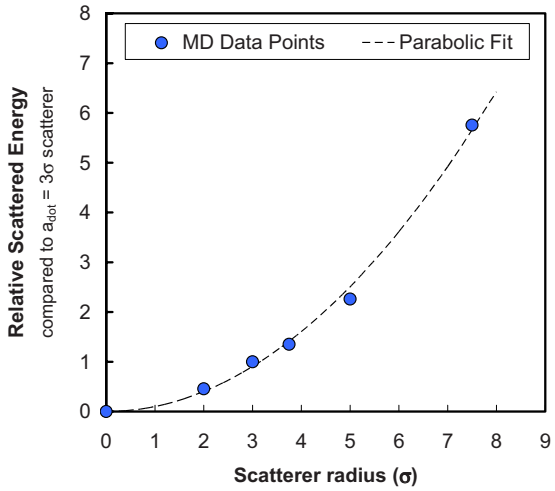


FIG. 23. (Color online) Trend of scattered energy vs scatterer size, $ka_{dot}=3$, rigid spherical scatterers.

the error associated with scaling results in a limitation on the accuracy of the approach. This limitation is flexible because as computational power continues to grow, progressively larger and more accurate models will become possible and the required degree of scaling will decrease.

The conditions required for scaling can be shown another way using the asymmetry factor $\langle\Phi\rangle$,[22]

$$\langle\Phi\rangle = \frac{1}{4\pi}\int_{4\pi\ str.} \Phi(\varpi)\cos(\theta)d\varpi. \tag{22}$$

The asymmetry factor is a convenient metric indicating the character of the scattering. It ranges from a maximum of 1, which indicates pure forward scattering, to a minimum of −1, which indicates pure backscattering at $\theta=180°$. A value of 0 indicates symmetric scattering relative to the $\theta=90°$ plane. The value of $\langle\Phi\rangle$ provides a sense of a scattering event's influence upon phonon transport, with very high $\langle\Phi\rangle$ values indicating minimal change in phonon-carried heat current following scattering and small or negative values indicating progressively greater scattering-induced disruption of the propagation of phonons along the $\theta=0°$ direction. Figure 22 shows the asymmetry factor for multiple cases with $ka_{dot}=3$. The figure illustrates that below a threshold value of $kA_{cell}\sim 1.5$, the relative forward and backward scattering levels of the phase functions are approximately constant. This provides another indication that scaling can be performed for sufficiently low $kA_{cell}$.

Scattering cross sections were also investigated by running a set of simulations for $ka_{dot}=3$, with various $a_{dot}$. The resulting scattered energy trend is shown in Fig. 23. The results show that the value of $\Sigma_s$ increases in proportion to $a_{dot}^2$, as expected from geometric scaling, and this supports the idea of using a scatterer cross section to describe the scattering events.

## VII. ADVANTAGES AND LIMITATIONS OF THE MODELING TECHNIQUE

The MD approach presented here has several advantages over alternative approaches in modeling elastic wave scattering in continuous media, and in some situations, may be more practical. The MD model enables all possible wave modes, unlike theoretical fluid acoustics, which treats only longitudinal modes in isotropic media. Analytical elasticity calculations handle both longitudinal and transverse modes, but for some cases with unusual scatterer shapes, strong anisotropy, and/or nonrigid scatterers, analytical solutions are either impractical or require numerical calculations to evaluate many terms and are thus no longer purely analytical solutions. For such cases, which can and do occur in real materials, an MD calculation is often a more straightforward and rapid alternative. It is fully three dimensional and also incorporates discrete masses and their effect on high-frequency dispersion, more complex and diffuse boundary definitions, directionally dependent anharmonic potential functions, irregular or roughened scatterers, and natural lattice strain due to the presence of an inclusion. These features are not represented in the above theoretical treatments nor in FDTD and FEM. The computational cost of the present approach is much less than in FEM and is comparable to that of FDTD.

MD models are also capable of resolving optical modes, although these modes have not yet been studied since they do not occur in the fcc crystals of this work. This simulation capability is an important distinguishing feature of MD for which there is no equivalent description and equation set in continuum acoustic theory. These nonacoustic waves can play an important role in governing energy transport at high temperatures and in strongly nonequilibrium systems.

Another advantage is that the scattering phase functions generated by the present technique are sufficiently detailed to serve as inputs into mesoscale models of phonon motion such as Monte Carlo simulations.[45–49] Such simulations can incorporate theoretical rates for phonon-boundary, phonon-phonon, and phonon-point defect scattering, but do not yet account for phonon scattering with nanoparticle inclusions. The scattering phase functions generated using the present technique could be used to feed polarization-, particle shape–, and incident direction–dependent scattering probabilities into Monte Carlo simulations of phonon transport.

This will be important in modeling phonon-nanoparticle scattering in systems such as semiconductor quantum dot superlattices that are too large to be treated by molecular dynamics alone.

The simulation technique selected has a number of drawbacks and limitations on the range of conditions that can be practically simulated. One's choice of computer and the computation time available both put a lower limit on the wave frequencies that can be modeled. The simulation cell must be large enough to resolve the wave packet prior to the scattering event and to allow it to pass through and leave the monitoring region before the arrival of the reflected leading edge of the packet and the arrival of periodic echoes of the packet. With a given number of oscillations of some selected amplitude, the packet length grows inversely proportional to $k$. If the simulation cell length (per side) is proportional to the packet length, and the number of simulation time steps is proportional to the packet length, then the computation time required will be proportional to $1/k^4$. Fortunately, the resulting lower limit on $k$ will be eased as computing power increases. The lowest wave numbers we have used so far are approximately $k_{max[100]}/10$ or $0.4\sigma^{-1}$.

The method of data processing involves spatial averages of pressures, velocity components, and stress components. For small values of $k$, this produces a fairly accurate description of the pressure at some point in space, as the pressure or velocity component gradient has a small magnitude. This Eulerian approach to tracking stress and velocity is selected to provide a direct analogy with acoustic theories describing scattering. At high values of $k$, the weighted-averaging technique may smooth out local gradients and yield poor results. This is a basic limitation of the method of using atomic-level stresses in a molecular dynamics model to study wave scattering. The highest values of $k$ used in this study equaled $k_{max}/2$. The most straightforward and effective solution to this averaging difficulty is to select data collection points at the equilibrium lattice locations of various atoms in a thick radial band. This then requires data collection at multiple radii and corresponding adjustments in the postprocessing calculations.

As stresses and velocities are only directly computed at atomic locations, the source data are interpolated to intermediate positions when necessary. Calculations of atomic displacements are also tied to discrete positions of atoms. The resolution of the amplitude–wave number plots is ultimately limited by this fundamental spatial resolution of the lattice. For large simulations, the data will have many elements, allowing long wavelength amplitudes (e.g., $k<0.1k_{max}$) to be well determined with good resolution in $k$. For the ranges of wave numbers studied thus far, typical spacing in $k$ points (the resolution) on the amplitude–wave number graphs is $0.6\sigma^{-1}$. This is coarser than desired for examination of waves with $\lambda$ in the range of $3\sigma-6\sigma$. The amplitude–wave number plots are only truly valid along the axes of symmetry where wave vector and group velocity vector are aligned, but they still allow an examination of the characteristics of the scattered waves. We have found it more practical to track the scattered wave content using frequency-amplitude diagrams.

The simulation uses wave propagation in a lattice of 0 K, with a local "temperature" elevation due to the wave packet. Similar simplifications were made in a phonon scattering study by Sinha *et al.*,[50] which used an ambient environment without thermal phonons. The application of the results of this MD method to real materials is only a valid approximation when the atomic motions at the selected temperature are small compared to the lattice spacing and lie in the region where the motion is close to harmonic. The use of this simulation technique to calculate $\Phi(\theta,\phi)$ and $\Sigma_s$ values in a lattice at an elevated temperature may be possible but would require careful extraction of background thermal noise using frequency analysis and would also require larger wave packet amplitudes, which would subject the wave packet to stronger phonon-phonon scattering effects during its travel. As a result, a high-temperature simulation of this type would be impractical, slow, and unlikely to yield satisfactory results.

Additionally, the simulations are classical. Except in the high-temperature limit, the lattice vibrations modeled are not directly equivalent to phonons, which arise from the quantum field theory (second quantization). However, as there is an incomplete theoretical understanding of phonon scattering from nanoparticles, studies of classical wave scattering provide an important first step in understanding phonon scattering from these particles. In the future, methods such as nonequilibrium Green's functions for phonons[51] may be able to make similar scattering predictions without invoking classical assumptions.

## VIII. CONCLUSIONS

A technique is developed for the simulation of three-dimensional elastic scattering events using molecular dynamics. Methods of analyzing the data are created and applied to simulation results to generate phase functions for multiple modes of vibration in a solid. The results capture the influences of anisotropy, mode conversion, and scatterer shape and size, including roughness. In the sample argon fcc lattice, the technique involved is of practical use for a range of wave numbers from 10% to 50% of $k_{max[100]}$, though it may be extended to lower $k$. Scaling and range of applicability are investigated, and a dependence of results on $kA_{cell}$ is seen for high $kA_{cell}$. It is seen that phase functions and cross sections scale well for cases with $kA_{cell}\leqslant 1.5$, which corresponds to $a_{dot}/A_{cell}>2$. This indicates that the results can describe scattering phenomena at length scales beyond those of typical molecular dynamics simulations. The scattering phase functions generated by this technique are sufficiently detailed to serve as inputs into mesoscale approaches, such as Monte Carlo simulation, that enable treatment of phonon transport processes at length scales longer than those accessible to molecular dynamics. These approaches can provide useful tools for investigating heat transfer in materials with nanometer-scale structures such as semiconductor quantum dot superlattices.

## ACKNOWLEDGMENT

This work was supported by National Science Foundation CAREER Grant No. CBET-0547588.

[1] S.-M. Lee, D. G. Cahill, and R. Venkatasubramanian, Appl. Phys. Lett. **70**, 2957 (1997).
[2] G. Chen, S. Q. Zhou, D.-Y. Yao, C. J. Kim, X. Y. Zheng, J. L. Liu, and K. L. Wang, Proceedings of 17th International Thermoelectrics Conference, Nagoya, Japan, 2001 (unpublished), p. 202.
[3] X. Sun, Z. Zhang, and M. S. Dresselhaus, Appl. Phys. Lett. **74**, 4005 (1999).
[4] A. Khitun, A. Balandin, and K. L. Wang, Superlattices Microstruct. **26**, 181 (1999).
[5] A. Balandin and O. Lazarenkova, Appl. Phys. Lett. **82**, 415 (2003).
[6] T. C. Harman, J. Taylor, M. P. Walsh, and B. E. LaForge, Science **297**, 2229 (2002).
[7] A. Balandin, J. Nanosci. Nanotechnol. **5**, 1 (2005).
[8] G. Chen, IEEE Trans. Compon. Packag. Technol. **29**, 238 (2006).
[9] L. D. Hicks and M. S. Dresselhaus, Phys. Rev. B **47**, 12727 (1993).
[10] L. Hicks, T. Harman, and M. Dresselhaus, Appl. Phys. Lett. **65**, 3230 (1993).
[11] L. D. Hicks and M. S. Dresselhaus, Phys. Rev. B **47**, 16631 (1993).
[12] A. Majumdar, Science **303**, 777 (2004).
[13] Y.-M. Lin and M. S. Dresselhaus, Phys. Rev. B **68**, 075304 (2003).
[14] J. L. Liu, A. Khitun, K. L. Wang, T. Borca-Tasciuc, W. L. Liu, G. Chen, and D. P. Yu, J. Cryst. Growth **227-228**, 1111 (2001).
[15] K. F. Hsu, S. Loo, F. Guo, W. Chen, J. Dyck, C. Uher, T. Hogan, E. Polychroniadis, and M. Kanatzidis, Science **303**, 5659 (2004).
[16] R. Venkatasubramanian, Phys. Rev. B **61**, 3091 (2000).
[17] W. Kim, J. Zide, A. Gossard, D. Klenov, S. Stemmer, A. Shakouri, and A. Majumdar, Phys. Rev. Lett. **96**, 045901 (2006).
[18] I. Sur, A. Casian, and A. Balandin, Phys. Rev. B **69**, 035306 (2004).
[19] A. Khitun, A. Balandin, J. L. Liu, and K. L. Wang, J. Appl. Phys. **88**, 696 (2000).
[20] R. Prasher, ASME J. Heat Transfer **125**, 1156 (2003).
[21] R. Prasher, ASME J. Heat Transfer **126**, 793 (2004).
[22] R. Prasher, J. Appl. Phys. **96**, 5202 (2004).
[23] R. Prasher, J. Appl. Phys. **97**, 064313 (2005).
[24] R. Prasher, ASME J. Heat Transfer **128**, 627 (2006).
[25] J. Callaway, Phys. Rev. **113**, 1046 (1959).
[26] W. Kim and A. Majumdar, J. Appl. Phys. **99**, 084306 (2006).
[27] A. Khitun, A. Balandin, J. L. Liu, and K. L. Wang, Superlattices Microstruct. **30**, 1 (2001).
[28] J. A. G. Temple, J. Phys. D **21**, 859 (1988).
[29] M. P. Allen and D. J. Tildesley, 1987, *Computer Simulation of Liquids* (Oxford University Press, Oxford, U.K.).
[30] C. F. Ying, and R. Truell, J. Appl. Phys. **27**, 1086 (1956).
[31] P. M. Morse and K. U. Ingard, *Theoretical Acoustics* (Princeton University Press, Princeton, NJ, 1968).
[32] P. K. Schelling, S. R. Phillpot, and P. Keblinski, Appl. Phys. Lett. **80**, 2484 (2002).
[33] J. R. Lukes and C.-L. Tien, Microscale Thermophys. Eng. **8**, 341 (2004).
[34] N. Zuckerman and J. R. Lukes, ASME J. Heat Transfer (to be published).
[35] V. Vitek and T. Egami, Phys. Status Solidi B **144**, 145 (1987).
[36] B. A. Auld, *Acoustic Fields and Waves in Solids* (Wiley, New York, 1973), Vol. I.
[37] J. M. Carcione, *Wave Fields in Real Media: Wave Propagation in Anisotropic, Anelastic, and Porous Media* (Pergamon/Elsevier Science Ltd., Kidlington, Oxford, U.K., 2001).
[38] J. A. Barker, M. L. Klein, and M. V. Bobetic, Phys. Rev. B **2**, 4176 (1970).
[39] J. D. N. Cheeke, *Fundamental and Applications of Ultrasonic Waves* (CRC, Boca Raton, FL, 2002).
[40] S. Volz and G. Chen, Physica B **263-264**, 709 (1999).
[41] J. E. Gubernatis, E. Domany, and J. A. Krumhansl, J. Appl. Phys. **48**, 2804 (1977).
[42] R. Siegel and J. Howell, *Thermal Radiation Heat Transfer* (Taylor & Francis, New York, 2002).
[43] N. Zuckerman and J. R. Lukes, Proceedings of HT2007, 2007 ASME-JSME Thermal Engineering Summer Heat Transfer Conference, Vancouver, BC, Canada, 8–12 July, 2007, Paper No. HT2007.32674.
[44] J. P. Wolfe, *Imaging Phonons: Acoustic Wave Propagation in Solids* (Cambridge University Press, Cambridge, England, 1998).
[45] R. B. Peterson, ASME J. Heat Transfer **116**, 815 (1994).
[46] S. Mazumder and A. Majumdar, ASME J. Heat Transfer **123**, 749 (2001).
[47] Y. Chen, D. Li, J. Lukes, and A. Majumdar, ASME J. Heat Transfer **127**, 1129 (2005).
[48] D. Lacroix, K. Joulain, and D. Lemonnier, Phys. Rev. B **72**, 064305 (2005).
[49] D. Lacroix, K. Joulain, D. Terris, and D. Lemonnier, Appl. Phys. Lett. **89**, 103104 (2006).
[50] S. Sinha, P. K. Schelling, S. R. Phillpot, and K. E. Goodson, J. Appl. Phys. **97**, 023702 (2005).
[51] W. Zhang, T. S. Fisher, and N. Mingo, Numer. Heat Transfer, Part B **51**, 333 (2007).